Superconductivity in twisted bilayer quasi-one-dimensional systems with flat bands

F. D. R. Santos and R. G. Dias
I3N & Departamento de Física, Universidade de Aveiro, Campus Universitário de Santiago, 3810-193 Aveiro, Portugal

(Received 1 July 2021; revised 1 October 2021; accepted 4 October 2021; published 18 October 2021)

Unconventional superconductivity recently observed in twisted bilayer graphene is associated with the presence of van-Hove singularities very close to the Fermi level reflecting the flattening of bands for a set of magic twist angles. In this paper, we address a stack of two identical quasi-one-dimensional layers, each one composed of a set of chains with p-wave orbitals at each site. When the layers are stacked with a 90° relative angle, the bilayer system resembles the Mielke lattice (which admits one exact flat band in the one-body tight-binding model for particular values of the hopping parameters). When a small rotation is applied to one of the layers, regions with different layer stacking appear that may be characterized as one-dimensional or two-dimensional regions according to the most relevant hopping integrals between layers. The system, for sizes smaller or of the order of the Moiré pattern unit cell, can be qualitatively described: (i) addressing individually each region, for example in what concerns the density of states, (ii) interpreting the full lattice as a coupled system of these regions. This generates a n-band model, where each band is associated to a particular region of the lattice. We address the role of these different regions on the upper critical field transition curve of a superconducting phase.

DOI: 10.1103/PhysRevB.104.165130

I. INTRODUCTION

Moiré patterns are interference patterns produced by the slight offset superposition of two identical two-dimensional (2D) periodic patterns. In physics, these patterns can be created by stacking thin sheets of atoms, bonded by weak Van der Waals interactions, and the resulting materials often have unusual electronic and optical properties [1]. One prime example is twisted bilayer graphene (TBG) [2–7]. Theoretical studies showed that when the twist between the two graphene sheets is reduced to small angles, the band velocity decreases, resulting in the flattening of bands [8–11]. This phenomenon was confirmed by the observation of two energy symmetric van-Hove singularities (vHSs) in the density of states (DOS) [12]. In reality, the width of the bands do not depend monotonically on the twist angle but for a set of "magical" angles the band velocity becomes zero [13–16], the energy difference between the vHSs reaches a minimum, and they are no farther than 10 meV from the Fermi energy [17]. The presence of vHSs near the Fermi level is known to enhance superconductivity correlations [18–21], and thus, one can expect to find a superconducting phase in TGB. Recently, inducing insulating and superconducting states were experimentally observed in TBG [2,3], and the underlying mechanisms behind them have since been discussed [22–25]. These states are absent in single graphene sheets and are very similar to those seen in copper-oxide-based high-T_c superconductors.

The flattening of bands that occurs in bilayer graphene upon twist motivated the study, reported in this paper, of new ways of constructing bilayer Hamiltonians that admit flat bands. Flat band systems have been extensively studied from a theoretical point of view in the last few decades, since the works of Mielke and Tasaki [26–30]. These are usually 2D tight-binding Hamiltonians (single layer) and the flat bands result from destructive interference in the single-electron paths and reflect the existence of compact localized states [31–33]. The respective lattices are often called decorated lattices. In this paper, we propose constructing a bilayer decorated lattice by stacking two copies of a quasi-one-dimensional (quasi-1D) layer composed of a set of equally spaced chains with p-wave orbitals at each site. When the layers are rotated 90° with respect to one another, for a certain interlayer distance (experimentally, this distance can be controlled by applying pressure to the layers [34–36]; for instance, such a method was used to control the magic twist angle in the TBG [37]) the intralayer and interlayer hopping terms between nearest neighbors are of the same order, and the system resembles a Mielke lattice, which admits one exact flat band in the single-particle tight-binding (TB) model (note that our model shows some common features with the TBG such as the presence of flat bands in the energy dispersion and the bilayer stacking, but it is structurally very different due to the strong anisotropy of the layers that can be described as weakly coupled 1D chains of p orbitals). We found that applying an additional small twist angle θ_t may be enough to modify considerably the electronic properties of the system, such as the density of states, and the form of the energy eigenstates. Subspaces of 1D states may emerge, associated with certain well defined regions of the lattice (in Sec. III, we describe the lattices corresponding to those regions), and the Mielke flat-band compact states may not survive. The size of the systems discussed in this work are of the order of the Moiré pattern unit cell (only a few unit cell are present at most), and Bloch theory is not useful to determine the electronic properties of such systems [13]. Instead, we describe qualitatively the twisted Mielke-like system as a set of regions with different stacking, each of them

with a particular band structure, so that the full band structure becomes that of a n-band model where each band is associated with different regions of the twisted lattice.

We study the superconductivity of this n-band model assuming intraband and weak interband pairing interactions. The latter reflects the tunneling of Cooper pairs between different regions and since different values of the twisting angle θ_t lead to different sizes and geometries of each stacking region, the relative values of the pairing interactions should also be a function of the twist angle. In our qualitative approach, we do not determine this dependence, but we consider different relative values for these pairing interactions that enhance the contribution of a particular band and consequently the contribution of a region with a particular stacking. Furthermore, in our superconductivity study, we will reduce the n-band model to simple qualitative two-band models that describe the existence of particular bands (associated with different stacking regions) with overlapping density of states (that may be 1D- or 2D-like, with or without vHSs) of the twisted system in particular energy intervals. Two particular cases are considered, and both of them include a band typical of an isotropic 2D conventional superconductor with an energy-band dispersion $\epsilon_k = v_F(k - k_F)$, where v_F is the Fermi velocity and k_F is the Fermi momentum: (i) In the first case, the isotropic 2D band overlaps with a band of a quasi-1D superconductor, with an energy-band dispersion $\epsilon_k - \mu = v_F(|k_x| - k_F) - 2t_y \cos(k_y)$, where t_y is very small, and k_x and k_y are, respectively, the momentum in the directions x and y; (ii) in the second case, the 2D band overlaps with a band with a van-Hove singularity. We adopt the isotropic dispersion relation $\epsilon_k - \epsilon_{vh} = a \times \text{sign}(q)|q|^b$, where $q = k - k_{vh}$, ϵ_{vh} and k_{vh} are, respectively, the energy and momentum at the van-Hove singularity respective to the flat band, and a and b are constant parameters that control the extension of the saddle point.

We discuss the role of the bands on the superconducting state, in particular by looking at the form of the upper critical field transition curve. In what concerns the first model, we found that the presence of the quasi-1D band modifies the form of the upper critical field transition curve from a paraboliclike curve, typical of a one-band 2D superconductor, to a curve that diverges at low temperatures reflecting a dimensional crossover typical of quasi-1D superconductors. For increasing quasi-1D intraband interaction, the temperature at which the field diverges becomes higher, and this behavior becomes true for temperatures close to the critical temperature T_c, given a large enough quasi-1D bandwidth. In the case of the second model we found that the curvature of the critical curve also starts to become positive at higher temperatures as one increases the intraband interaction of the band with a van-Hove singularity. In this case, in the temperature range where the curvature of the critical curve is positive, the decay of the field with temperature is power-law. The numerical calculations of the upper critical fields are carried out using a Lanczos approach introduced in Refs. [38,39] for one band but generalized by us in this paper to a n-band system (see Appendix D). This paper is organized in the following way. In Sec. II, we introduce the Hamiltonian that describes the bilayer Mielke-like lattice. In Sec. III, we present the lattice stacking configurations corresponding to the different regions obtained when a twist is applied to the bilayer Mielke-like lattice and discuss their dimensionality. In Sec. IV, we show the density of states for $\theta_t = 0^\circ$, for all those different lattice stackings, and describe particular energy eigenstates. In Sec. V, we identify the regions associated to the subspaces of 2D and 1D states for $\theta_t = 2^\circ$ and $\theta_t = 5^\circ$, starting from two different lattice configurations, and describe particular energy eigenstates. In Sec. VI, we present the results for the upper critical field-vs-temperature phase diagram for the two band models described above. In Sec. VII, we leave our final remarks. In Appendix A, we show how to decompose a rotated p_y orbital into a sum of p_x and p_y orbitals. In Appendix B, the n-band gap equation is derived and the expressions for the pair propagator for the superconductors corresponding to one-band systems with a 2D band, a quasi-1D band, and a band with a van-Hove singularity are given. In Appendix C, we introduce the n-band gap equation in the mixed representation. In Appendix D, we show how to simplify the n-band gap equation by discretizing it in one of the directions and present the Lanczos method used to solve that equation.

II. MODEL

We consider a single-particle tight-binding (TB) model for a system of two stacked quasi-1D layers, rotated 90° in relation to each another, each composed of a set of equally spaced chains of identical atoms. In order for this system to resemble the Mielke lattice, the hopping terms between first neighbors in each chain and between the nearest atoms of different layers should be the dominant ones, and hopping of particles between chains of the same layer should be negligible. However, the distance between adjacent atoms of adjacent chains is of the order of the distance between first-neighbor atoms in each chain (we assume it to be the same, see Fig. 1). In order for these hoppings terms to be neglected, we consider that the orbitals associated to the atoms of layers 1 (bottom layer) and 2 (top layer) are, respectively, p_x and p_y orbitals (see Fig. 1). This implies that the hopping energies depend not only on the distance between the center of the orbitals but also on their relative orientation. The energies associated to intralayer hoppings are given by the following [40]

$$V_{x,x} = l^2 V_{pp\sigma}(d) + (1 - l^2) V_{pp\pi}(d), \tag{1}$$

where $l = (x_1 - x_2)/d$, with x_1 and x_2 being the x coordinates of the mass center of each orbital, d the distance between those centers, and $|V_{pp\sigma}| > |V_{pp\pi}|$ for the same distance (to determine $V_{y,y}$ one simply does $x \to y$). For hoppings between nearest neighbor orbitals in a chain, one has $l = 1$ and so $V_{x,x} = V_{pp\sigma}(d = r_0)$, where r_0 is the distance between nearest neighbor orbital in a chain. For hoppings between adjacent orbitals of adjacent chains, one has $l = 0$ and so $V_{x,x} = V_{pp\pi}(d = r_0)$. The neglecting of $V_{pp\pi}(d = r_0)$ is qualitatively justified if all relevant energy scales are larger than this value, that is, for example, when the thermal energy is larger than $V_{pp\pi}(d = r_0)$. In the following, we will adopt this approximation, that is, any hopping terms associated to energies equal or below $V_{pp\pi}(d = r_0)$ are not considered in the Hamiltonian. Thus, the tight-binding Hamiltonian for our

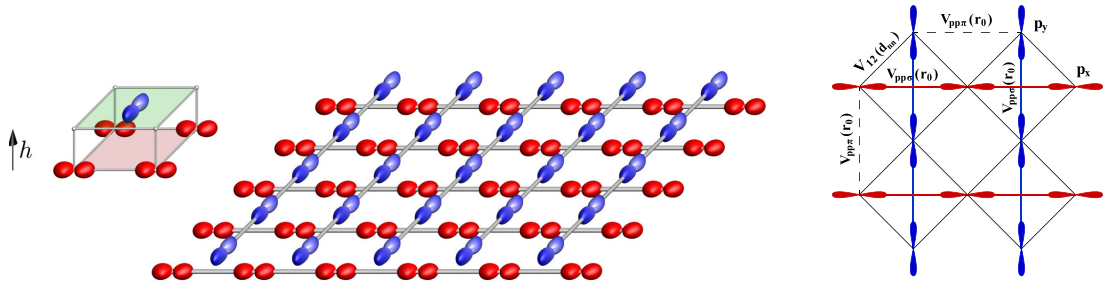

FIG. 1. Our Mielke-like lattice consists of a stack of two identical quasi-1D layers rotated 90° in relation to one another, each composed of a set of equally spaced chains with either p_x (red ellipsoids) or p_y (blue ellipsoids) orbitals as shown in the center diagram. The intralayer hopping interactions, in each chain, in layer 1 (horizontal layer) and layer 2 (vertical layer stacked on top of layer 1) are represented by red and blue lines, respectively, in the right diagram. The distance between layers, h, as shown in the left diagram, is chosen such that the intralayer and interlayer (black lines) hopping parameters between nearest-neighbor orbitals are equal. Intralayer hopping terms between the nearest orbitals of different chains (dashed black lines) are very small and will not be included in the Hamiltonian.

Mielke-like system is given by

$$H_{TB} = H_1 + H_2 + H_{12}, \tag{2}$$

with

$$H_1 = V_{pp\sigma}(r_0)\sum_{i=1}^{N_1}\sum_{j=1}^{L_1} a^\dagger_{i,j}a_{i,j+1} + a^\dagger_{i,j}a_{i,j-1} + \text{H.c.}, \tag{3}$$

and

$$H_2 = V_{pp\sigma}(r_0)\sum_{i=1}^{N_2}\sum_{j=1}^{L_2} b^\dagger_{i,j}b_{i,j+1} + b^\dagger_{i,j}b_{i,j-1} + \text{H.c.}, \tag{4}$$

where H_1 and H_2 correspond to hopping terms between nearest neighbor orbitals in each chain of layer 1 and layer 2, respectively. $N_1(N_2)$ is the number of chains in layer 1(2) and $L_1(L_2)$ is the number of atoms in each chain of layer 1(2). In this work, we chose to use the parameters given in [41]: $V_{pp\sigma}(d = r_0) = -3.06$ and $V_{pp\pi}(d = r_0) = 0.87$ (these values correspond to the parameters for a diamond structure).

The interlayer Hamiltonian H_{12} includes the hopping terms $V_{12}(d)$ between orbitals from different layers (that are at a distance d from each other) that are larger than the cutoff value indicated above, and it has a different form for each of the possible stackings of the two layers. In the case of the Mielke-like stacking shown in Fig. 1, this Hamiltonian has the form

$$H_{12} = V_{12}(d_{nn})\sum_{i=1}^{N_1}\sum_{j=1}^{L_1} a^\dagger_{i,j}b_{i,j} + a^\dagger_{i,j}b_{i+1,j} + a^\dagger_{i,j}b_{i,j+1} + a^\dagger_{i,j}b_{i+1,j+1} + \text{H.c.}, \tag{5}$$

where d_{nn} is the diagonal distance between nearest neighbor sites in different layers, as one can conclude from the discussion below. The (i, j) orbitals of layer 2 are obtained from the (i, j) orbitals of layer 1 applying an in-plane translation of $(-r_0/2, -r_0/2)$, an out-of-plane (transverse) h shift, and a 90° clockwise rotation.

We know that CL states associated to a flat band exist in the band structure of the Mielke lattice if the hopping parameters $V_{pp\sigma}(r_0)$ and $V_{12}(d_{nn})$ shown in Fig. 1 are all exactly the same. Then, in our system, we have to enforce that the hopping energies between nearest neighbor atoms of different layers, $V_{12}(d_{nn})$, have to be equal to $V_{pp\sigma}(r_0)$. Hoppings between atoms of different layers implies, in our case, a Hamiltonian matrix element between p_x and p_y orbitals. The energy associated with such hopping terms is given by [40]

$$V_{xy} = lmV_{pp\sigma}(d) - lmV_{pp\pi}(d), \tag{6}$$

where again $l = (x_1 - x_2)/d$ and $m = (y_1 - y_2)/d$, with y_1 and y_2 being the y coordinates of the mass center of the two orbitals, and $V_{pp\sigma}(d)$ and $V_{pp\pi}(d)$ being functions of distance of the form $V_{pp\sigma}(d) = V_{pp\sigma}(r_0)(r_0/d)^n$ [and $V_{pp\pi}(d) = V_{pp\pi}(r_0)(r_0/d)^n$] [41,42], where the power factor $n = 2$ was chosen according to Refs. [41,42]. The distance between layers, h, is given by

$$h = \sqrt{d_{nn}^2 - 2(r_0/2)^2}, \tag{7}$$

where d_{nn} can be obtained from $V_{xy}(d = d_{nn}) = V_{pp\sigma}(d = r_0)$, that is,

$$[lmV_{pp\sigma}(r_0) - lmV_{pp\pi}(r_0)](r_0/d_{nn})^n = V_{pp\sigma}(d = r_0). \tag{8}$$

The conditions for the construction of a Mielke-like lattice are all settled. When we apply a rotation, the distance between atoms of different layers changes and the orientation of the orbitals on the rotated layer also changes, and these are no longer p_y orbitals. However, we can decompose the new orbitals, $|p_{y'}\rangle$, into a combination of p_x orbitals, $|p_x\rangle$, and p_y orbitals, such that $|p_y\rangle$, $|p_{y'}\rangle = \cos\theta_t\,|p_y\rangle + \sin\theta_t\,|p_x\rangle$ (see Appendix A for details), and the interlayer hopping energies are now given by

$$V_{xy'} = \cos(\theta_t)V_{x,y} + \sin(\theta_t)V_{x,x}. \tag{9}$$

In our work we chose to fix layer 1 and rotate layer 2, with the rotation axis being transversal to the plane of layer 2, crossing it at the geometric center, which coincides with the center of one of the Mielke plaquettes, and thus the rotation axis will not cross through any atom of the lattice. Nonetheless, we tested a scenario where the rotation axis crosses an atom of layer 2, and for small twist angles no noticeable differences where found in our results. We also tested what happens if the rotation axis crosses one or two unit cells far apart from the geometric center, and the same applies. Take note that we choose to rotate layer 2 in the anticlockwise direction, and in

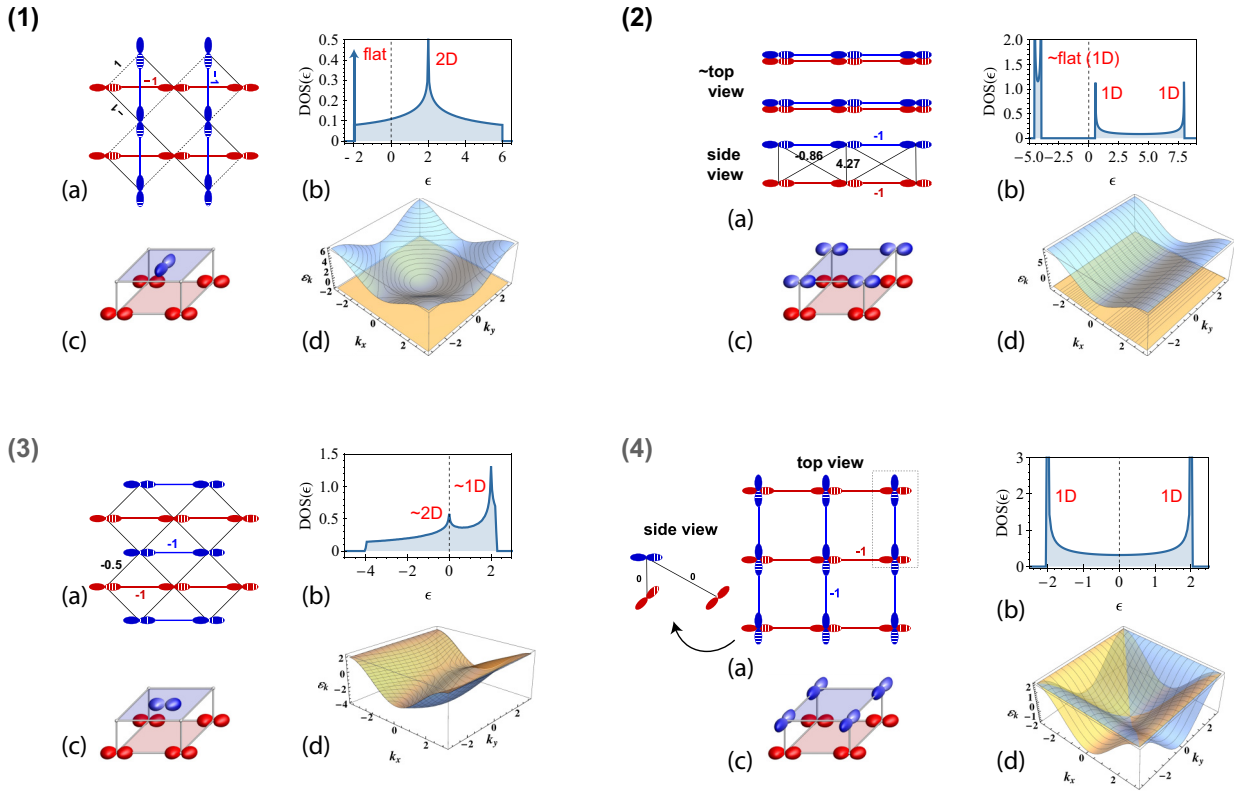

FIG. 2. (a) The first four of the eight possible orbital stackings described in the main text one may find in the Moiré pattern of the twisted system. We have assumed in all of them the same interlayer distance as in the Mielke-like stacking. The hoppings parameters are normalized to the nearest neighbor hopping parameter along the chains. (b), (c), and (d) show, respectively, the corresponding density of states, unit cell, and electronic band structure. In (b), each van-Hove singularity is labeled according to whether it has a decay typical of a 2D or a 1D band, where the symbol "∼" preceding some of those labels stands for "quasi."

contrast with TBG, our results, due to the anisotropic nature of the p orbitals, depend on the direction chosen.

Remember that an important condition for the construction of the Mielke-like lattice was to impose that hopping terms between orbitals in adjacent chains of the same layer have to be neglected (if we include these terms in the Hamiltonian, the flat band becomes slightly dispersive). Thus, when we twist the system, we calculate all the hopping energies and only take into account terms larger than a certain cutoff V_{cutoff}, which should be larger than $|V_{pp\pi}(r_0)| = 0.87$, i.e.,

$$\cos\theta_t(lmV_{pp\sigma}(r_0) - lmV_{pp\pi}(r_0))(r_0/d)^n + \sin\theta_t(l^2V_{pp\sigma}(r_0) + (1-l^2)V_{pp\pi}(r_0))(r_0/d)^n > V_{\text{cutoff}}. \tag{10}$$

The choice of V_{cutoff} will be discussed in Sec. III.

III. MIELKE-LIKE LATTICE AND OTHER LATTICE ARRANGEMENTS DIMENSIONALITY

When we apply a twist, the arrangement of the orbitals of layer 2 in relation to the ones of layer 1 changes throughout the lattice. Moire patterns form, reflecting regions with different atom stacking. These regions can either be 1D- or 2D-like [i.e., orbitals of layer 2 may have hopping terms for orbitals belonging to only one chain (1D) or to more than one chain (2D) of layer 1 or vice versa] and they will be similar to one of the stackings shown in Figs. 2 and 3 (or to an intermediate case between those). We classify them according to whether the 1D chains in the two layers are perpendicular or parallel to each other and on whether the orbitals of the two layers are superimposed or intercalated. In the cases where the orbitals are intercalated, we distinguish them according to the in-plane translation vector of layer 2 relatively to layer 1. So, we have

(1) perpendicular intercalated, $(1/2, 1/2)r_0$ (Mielke-like lattice);
(2) parallel superimposed (Creutz ladder-like lattice);
(3) parallel intercalated, $(1/2, 1/2)r_0$;
(4) perpendicular superimposed;
(5) parallel intercalated, $(1/2, 0)r_0$;
(6) parallel intercalated, $(0, 1/2)r_0$;
(7) perpendicular intercalated, $(1/2, 0)r_0$;
(8) perpendicular intercalated, $(0, 1/2)r_0$.

All these stackings, as well as the respective density of states, unit cell, and electronic band structure, are shown in Figs. 2 and 3.

According to Eq. (6), the lowest finite value for the nearest neighbor hopping interlayer interactions, $t_{nn,12}$, occurs in case (3), with $t^{(3)}_{nn,12} \approx 0.5V_{pp\sigma}$. We will then consider only interlayer hopping terms with energy values larger than a certain cutoff energy which is slightly smaller than $t^{(3)}_{nn,12}$. To be precise, we consider that the hopping parameters t_{12} in H_{12}

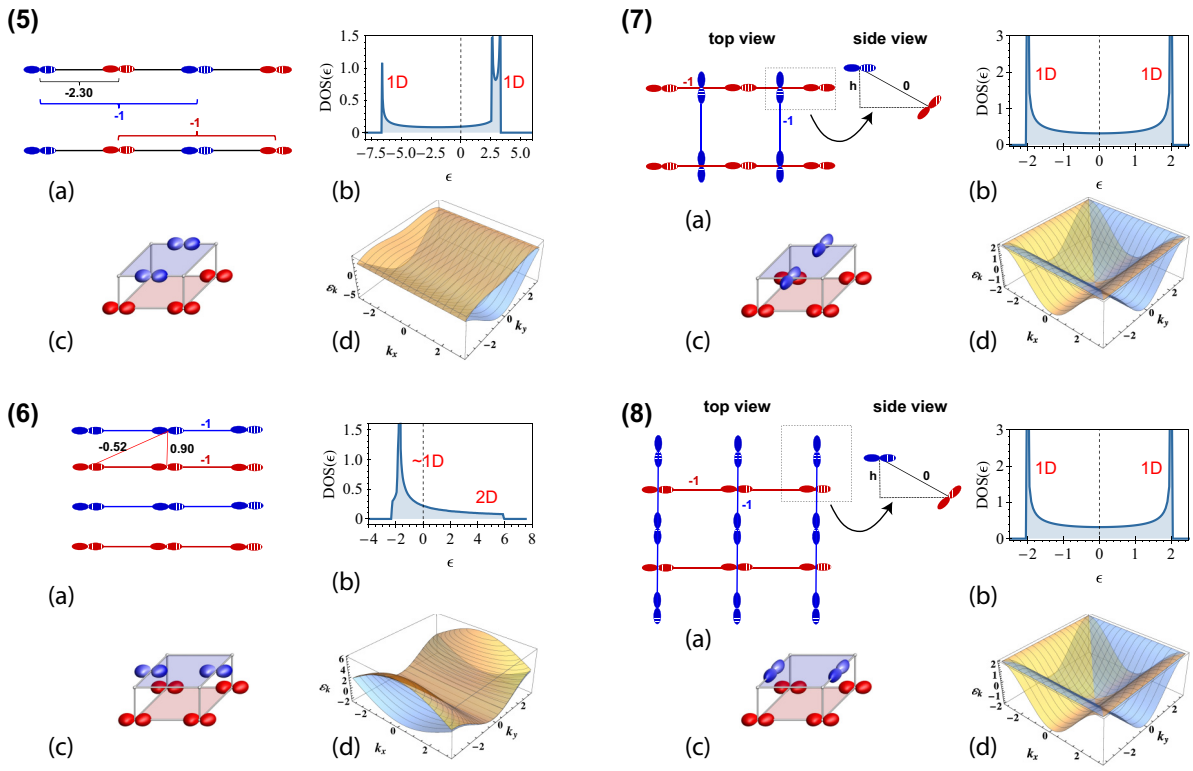

FIG. 3. (a) The last four of the eight possible orbital stackings described in the main text. (b), (c), and (d) show, respectively, the corresponding density of states, unit cell, and electronic band structure. The description of the figure is the same as in Fig. 2.

should obey the following condition

$$t_{12}^{\text{terms}} \geqslant V_{\text{cutoff}} = \frac{V_{pp\sigma}}{2.1}. \tag{11}$$

Let us now discuss these eight lattice configurations, shown in Figs. 2 and 3, focusing on their dimensionality. The first case corresponds to the Mielke-like lattice already discussed. In (2) of Fig. 2, in agreement with the condition in Eq. (11), second neighbors interlayer hopping terms are considered, and the lattice resembles the Creutz ladder, and as such we expect to find 1D states. In (3) of Fig. 2, the position of the orbitals is the same as in the Mielke-like lattice, but the orbitals of layer 2 are in this case also p_x. Consequently, the interlayer hopping energies differ from those of the intralayer hopping terms, and the condition for the appearance of exact flat bands is broken. In (4), (7), and (8) of Figs. 2 and 3, there are no interlayer hopping terms between nearest neighbors because one of the orbitals is placed orthogonally on top of the chain of the other layer. The next neighbor interlayer hopping terms are too small to be considered, according to Eq. (11), and thus the layers are independent from each other, and consequently these systems are 1D. In (5) of Fig. 3, there are finite hopping terms between layers. However, since the layers are superimposed, the two first neighbor orbitals of each orbital of layer 2 belong to the same chain of layer 1, and then we also expect to find 1D states. Finally, in (6) of Fig. 3, the nearest-neighbor orbitals of each orbital of layer 2 belong to two adjacent chains of layer 1 and thus, in this case, the system is 2D. Note that Eq. (11) implies that in (6) of Fig. 3, next-nearest neighbor interlayer hopping terms have to be considered. In this case, the two next-nearest neighbors of each orbital belong to different chains. Since the system assuming only nearest neighbor interlayer interactions is already 2D, in the context of our qualitative model, the differences resulting from the inclusion of these additional terms are not relevant.

Furthermore, note that we did not take into account screening effects, which could reduce the next-neighbor or higher-neighbor hopping parameters to values below the ones shown in Figs. 2 and 3. This implies that in a more precise model of our system, the results would be more robust to variations of the chosen cutoff. As a last simplification in our model, we also neglected the fact that the orientation of the orbitals may change as a result of the overlap between chains, and instead we assumed that the orientation of the orbitals is always the orientation of the chain that it belongs to.

IV. DENSITY OF STATES FOR EACH STACKING

In Figs. 2(b) and 3(b), the density of states (DOS) $g(\epsilon)$ is shown for the eight stacking configurations. We have assumed in all of them the same interlayer distance as in the Mielke-like stacking (this interlayer distance can be controlled by applying a uniaxial pressure to the bilayer system), but if this condition is relaxed we still expect similar qualitative behavior of the DOS for each stacking.

For the Mielke-like lattice, (1) in Fig. 2, the DOS is similar to that of a 2D square lattice but with a particular feature, a singular peak centered at $\epsilon = -2$ which indicates the presence of a flat band in the electronic band structure. This band is associated to a subspace of compact localized states, i.e., states with finite amplitudes, only in a few orbitals localized

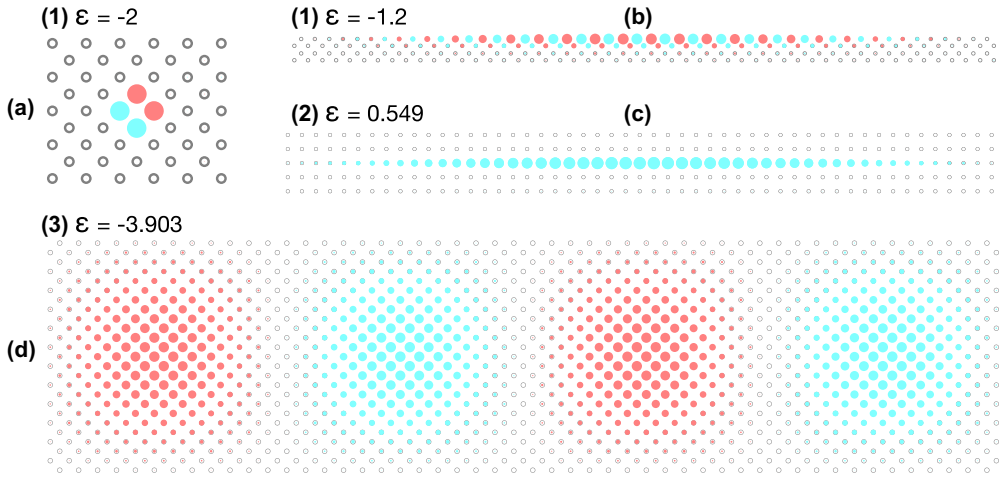

FIG. 4. Examples of energy eigenstates found in finite size lattices with stackings (1), (2), and (3). The wave function is finite in sites in color (with blue and red corresponding to positive and negative values, respectively, and the relative absolute value of the amplitudes being given by the circle radius). (a) Compact localized state in the Mielke-like lattice. The wave function has finite amplitude only in a small region of the lattice. (b) Edge state in a finite size Mielke-like lattice. (c) One-dimensional state in the Creutz ladderlike lattice. The wave-function amplitude is finite only in sites belonging to a certain chain. (d) Two-dimensional state in the (3) stacking lattice (the pattern repeats itself in the rest of the lattice).

in a small compact region of the lattice and zero in the rest [see Fig. 4(a) for an example]. In a finite size lattice, the DOS will additionally show a small peak due to the existence of a set of edge states. These states are characterized by having finite amplitude only at orbitals located at the edges of the lattice [see Fig. 4(b) for an example].

For the Creutz ladderlike ladder, (2) in Fig. 2, the DOS has as expected a region that is typical of a 1D band ($0.5 > \epsilon > 8$) and a region associated to a quasiflat 1D band ($-4.5 > \epsilon > -4$). In (5) in Fig. 3, $g(\epsilon)$ is also described by two regions associated to 1D bands but with some overlap. In both cases we find large subspaces of states with finite amplitude along one chain and zero in the rest of the lattice [see Fig. 4(c)].

In (3) in Fig. 2, the DOS is described as the overlap of a large 2D-band-like region with 2D states like the one shown in Fig. 4(d) and a small 1D-band-like region with states similar to those found in (2) and (5). Although the lattice arrangement is the same as in (1), this lattice does not support localized states.

In the case of (4), (7), and (8) in Figs. 2 and 3, as we mention in Sec. III, we do not have hopping between orbitals in different layers. Consequently, the DOS are typical of 1D bands. Since the layers are orthogonal to each other, one finds states that are 1D at either the x or the y direction.

In the case of (6) in Fig. 3, one can conclude from the electronic band structure that the van Hove singularity around $\varepsilon_k \sim -2$ is quasi-1D since the energy dispersion in the k_x direction is very small (and paraboliclike in the k_y direction). However, for energies close to the maximum of the top band, the behavior is 2D-like since one observes strong energy dispersion in both directions in the electronic band structure.

V. TWISTED LATTICES ELECTRONIC STATES AND DIMENSIONALITY

In the case of large systems (in our numerical analysis, each layer is composed of 50 chains with 50 orbitals each), even small rotations applied near the geometric center translate into considerable relative displacements between layers in the peripheral regions of the lattice. Then, upon a small twist, despite the stacking being very similar to that of the unrotated lattice in a region close to the rotation axis, it varies along the lattice, and different regions can be identified according to the orbitals stackings. In our system, as mentioned in Sec. III, these different arrangements will be similar to one of the other seven lattice stackings. Remember that while some of those stackings are 2D-like, others correspond to quasi-1D systems or can support flat-band states, and so, even for small rotations, it is possible to have a lattice with regions associated to 2D, quasi-1D, or flat-band states.

In Figs. 5 and 6, we identify the 2D and 1D regions on the twisted lattices, for $\theta_t = 2^\circ$ and $\theta_t = 5^\circ$, starting from stackings (1) and (2), and discuss some particular subspaces of states. Colors help identify the dimensionality in each region of the lattices. The red points correspond to the orbitals of layer 1. The orbitals of layer 2 are represented either by blue dots if they have hopping terms (or no terms at all) to orbitals of a single chain of layer 1 or by green dots if they may hop to orbitals that belong to different chains of layer 1. The colors are determined according to the H_{12} terms calculated using Eq. (9). In the same figure, for comparative purposes, we also present a similar color scheme but this time the dimensionality depends on the interlayer distances between orbitals. In this case, an orbital in layer 2 is represented by a green dot if it obeys the following condition (and by a blue dot otherwise):

$$\frac{d_{nn,12,2nd}}{d_{nn,12}} \leqslant 1.5, \tag{12}$$

where $d_{nn,12}$ is the distance from that orbital to the nearest neighbor in layer 1 (let us label the respective chain as A), and $d_{nn,12,2nd}$ is the distance to the nearest neighbor of the layer 1 that is not in chain A. In what concerns the unrotated cases, only in (8) the dimensionality of the lattice differs, being 1D in the former and 2D in the latter.

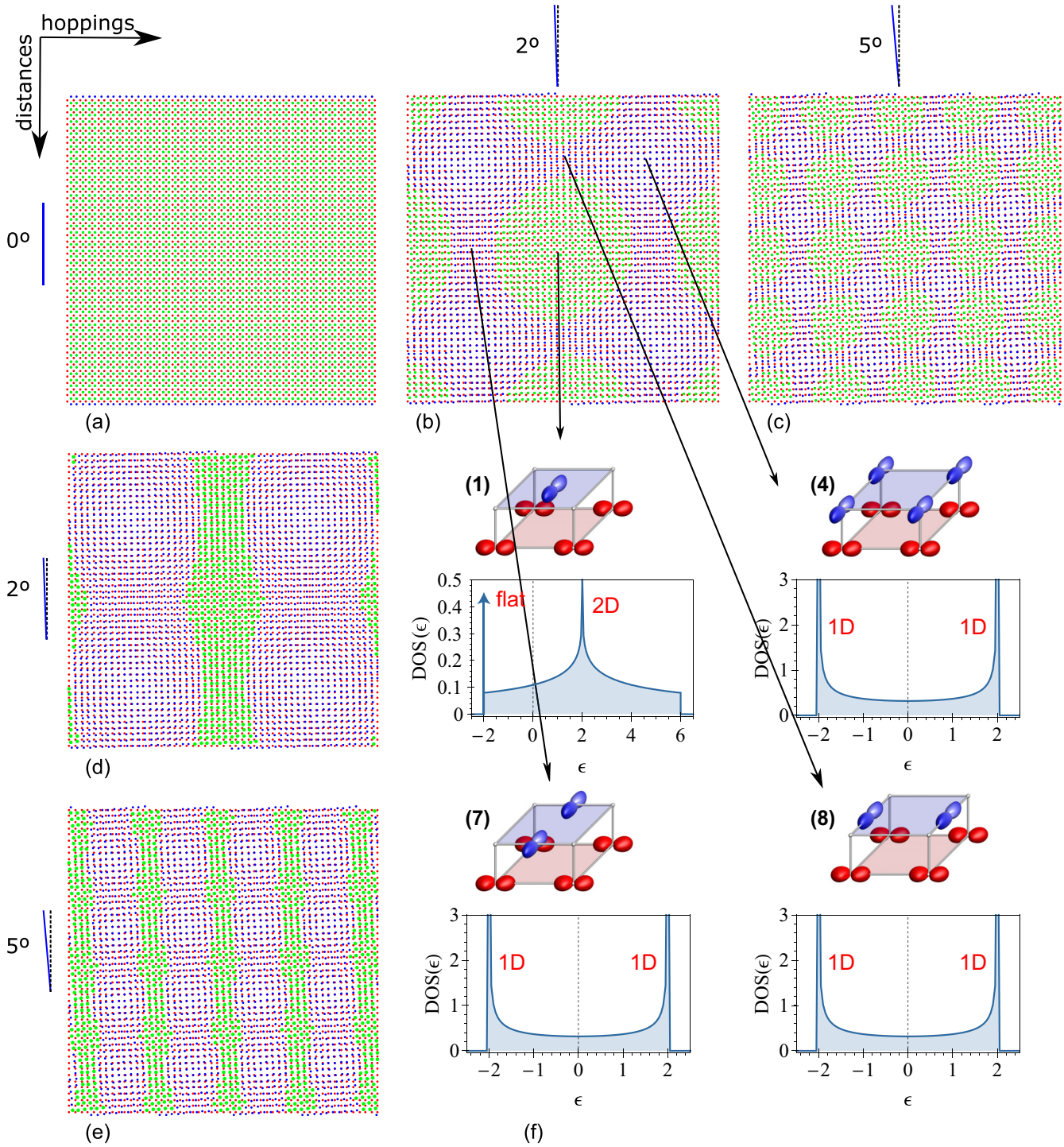

FIG. 5. Mielke-like lattice with a twist angle of layer 2 of: (a) $\theta_t = 0°$; (b) and (d) $\theta_t = 2°$; (c) and (e) $\theta_t = 5°$. Red dots represent the sites of layer 1. Sites of layer 2 represented by green dots correspond to 2D regions while blue dots correspond to 1D regions. (b),(c) Lattice configurations for $\theta_t = 2$ and $\theta_t = 5$ with the dimensionality of the sites being determined according to the hopping terms calculated using Eq. (9). In (d) and (e), the dimensionality of the sites is determined by Eq. (12). From (a) to (b),(c) and (a) to (d),(e) the green and blue regions occur with smaller periodicity. Each region has a lattice stacking indicated by the unit cells shown.

In Fig. 5, we show the Mielke-like lattice for several twist angles. For $\theta_t = 2°$ [see Fig. 5(b)], the position of the orbitals belonging to layer 2 in a region close to the center (green circlelike region in the center) of the lattice does not change significantly and thus the states associated to that region are 2D. At the left/right and top/bottom of that region, the bilayer system has (7) and (8) stackings, respectively (blue-red "bridges"), and thus these regions should support 1D states. These (7) and (8) stacking regions "converge" to regions with the stacking (4) which is also 1D-like (blue-red large regions). In the "distances only" color scheme [see Fig. 5(d)], regions with configuration (8) (above and

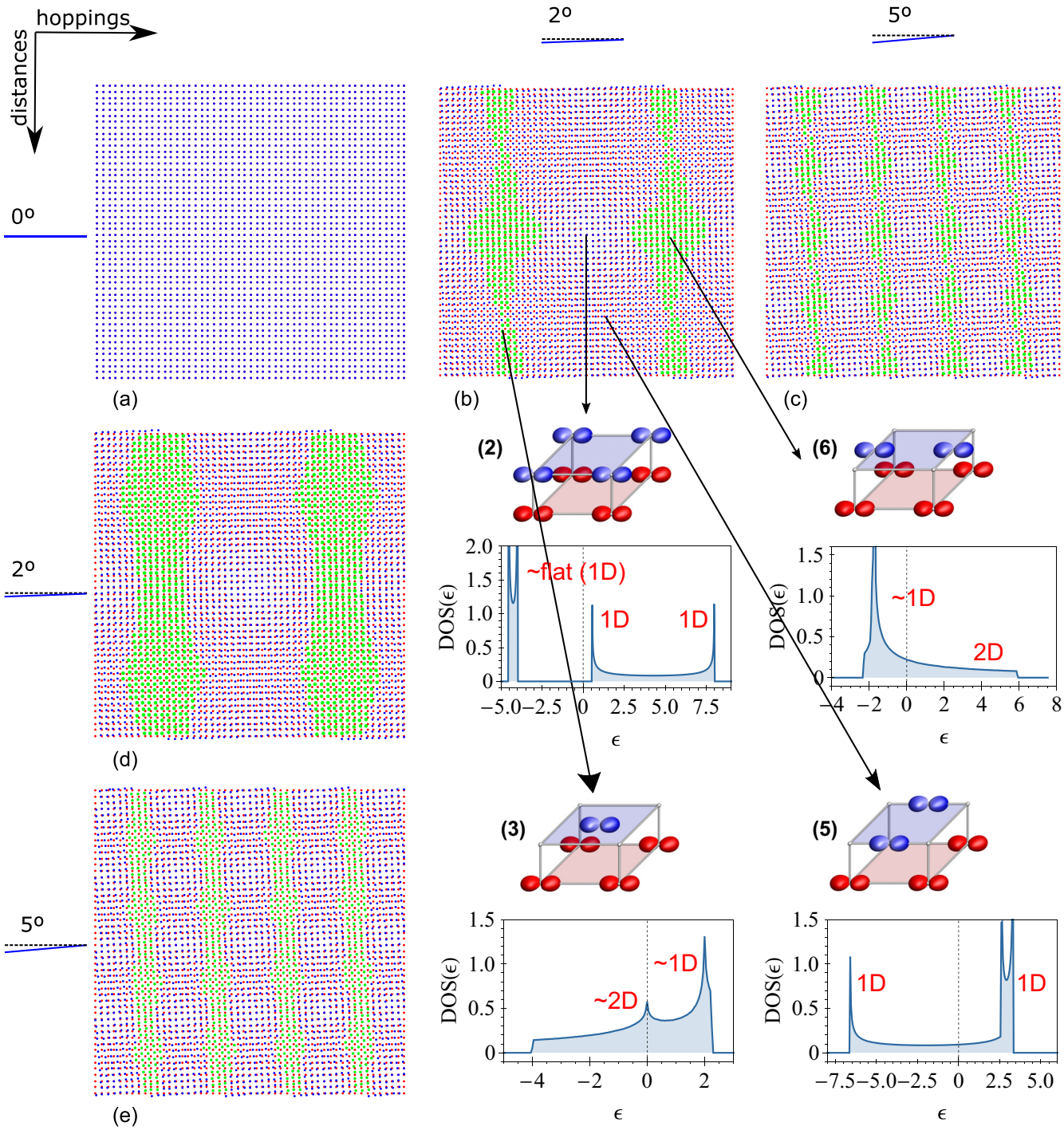

FIG. 6. (Creutz ladderlike lattice with a twist angle of layer 2 of: (a) $\theta_t = 0°$; (b) and (d) $\theta_t = 2°$; (c) and (e) $\theta_t = 5°$. The coloring follows the same reasoning as Fig. 5 (2D regions in green and 1D regions in blue). In (b) and (c) the dimensionality of the sites is determined according to the hopping terms calculated using Eq. (9). In (d) and (e), the dimensionality of the regions is determined by Eq. (12). As the twist angle increases, the green and blue regions occur with shorter periodicity.

below the center of the lattice) are 2D-like and as such, we have a 2D region that crosses vertically the middle region of the lattice. On the other hand, the 2D regions at the center, middle of the edges, and corners of the lattice are smaller.

In Fig. 7, we show the form of particular states that corroborate the dimensionality description reflected by the color schemes in Figs. 5 and 6. The state shown in Fig. 7(a) corresponds to a 2D state of the Mielke-like lattice, with $\theta_t = 2°$ and energy $\varepsilon = 5.84$ that has finite wave-function amplitude in the green region at the center of the lattice and zero in the rest of the lattice. Looking at Fig. 5, one can confirm that for energies $\varepsilon \sim 5.84$, only 2D regions have finite DOS and therefore the 1D regions behave as effective potential barriers.

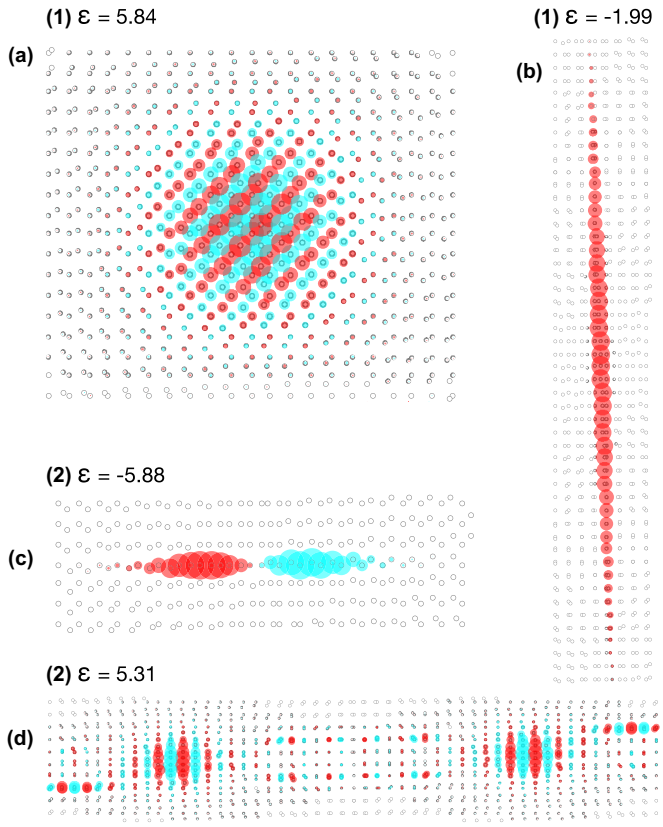

FIG. 7. (a),(b) Examples of energy eigenstates in the Mielke-like lattice, with $\theta_t = 2^\circ$. (a) 2D state located at the region with stacking (1) in the center of the lattice. Similar states can be found in the other red-green regions of Fig. 5(b). (b) 1D energy eigenstate with support in the left region of Fig. 5(b) with stackings (7) and (8). Note the deviation from the vertical direction due to the change of stacking. (c),(d) Examples of energy eigenstates in the Creutz ladderlike lattice, with $\theta_t = 2^\circ$. (c) 1D energy eigenstate in the region with stacking (5). In this case, there are no fully blue chains and thus we only find 1D states in a fraction of a chain. (d) Stripelike state in the central region of Fig. 6(b) that has support in the contiguous 1D and 2D regions and that is a linear combination of 1D and 2D states.

Similar states can be found at the middle of the edges or at the corners.

In Fig. 7(b), a 1D state of the Mielke-like lattice with $\theta_t = 2^\circ$ and energy $\varepsilon = -1.99$ is shown. In this case, the state has support vertically through a chain of layer 2, but one can also find horizontal 1D states along chains of layer 1.

For a slightly larger twist, $\theta_t = 5^\circ$, the periodicity of Moire patterns of the twisted Mielke-like lattice decreases [Fig. 5(c)], but the same regions as for $\theta_t = 2^\circ$ can be identified in the pattern. In the "distances only" color scheme [Fig. 5(e)], one sees again that the vertical bridges become 2D-like, but the 1D regions in the Moire pattern are larger. A further increase of the twist leads the 2D and 1D regions to become even more intercalated.

Next, we discuss the twisting of the Creutz ladderlike lattice, that is the stacking (2). When we apply a small twist of $\theta_t = 2^\circ$, we obtain the color schemes shown in Figs. 6(b) and 6(d). Naturally, in a region around the center, the atoms' stacking is very close to the unrotated case (2) and, as such, this region is associated to 1D states. Below and above this region, the stacking of the orbitals is similar to that of (5), which also supports 1D states. At the left and right of center, the lattice structure is close to that in (6) which supports 2D states. As one approaches the edges, the lattice arrangement tends to (2). There are some small regions around the 2D green region, where the orbitals are organized closely to (3), which is a 2D-like structure, but some of the sites of layer 2 are represented by blue dots. This can be understood by the fact that the choice of the hopping cutoff was done such that it would be sightly smaller than the nearest neighbor hopping energy of (3) (in the "distance only" [see Fig. 6(d)] color scheme this problem does not occur, and the green regions are wider). We could have chosen a smaller value for the cutoff, but then this value would be close to the second nearest neighbor hopping energies for (7) and (8) and the 1D-like behavior of such structures would be more easily, upon rotations, changed to 2D-like.

From the color schemes in Fig. 6, we conclude that the lattice is for the most part 1D and indeed we find 1D energy eigenstates with finite amplitudes in a section of a chain located between two 2D regions (similar states can also be found located between a 2D region and the closest edge of the lattice) [see Fig. 7(c)]. We also find states that have support in contiguous 1D and 2D regions. These states are stripelike states and are linear combinations of 1D and 2D states. In Fig. 7(d), we show one of these states with energy $\varepsilon = 5.31$, that is with energy in a range where the 1D DOS of stacking (2) overlaps with the DOS of stacking (6), see Fig. 6(b). It is due to this overlap that the linear combination of 1D and 2D states occurs in the energy eigenstate.

Just like in the previous cases, increasing the twist (but still in the range of small rotations), increases the periodicity of the 1D and 2D regions [see Figs. 6(c) and 6(e)]. One should note that the previous description of the twisted Mielke-like lattice and of the twisted Creutz ladderlike lattice covers also the cases where the twist is applied starting from one of the other six stackings, since one can apply a translation to the Moire patterns of Figs. 5 and 6 so that the chosen stacking occupies the central lattice region.

VI. SUPERCONDUCTING CRITICAL FIELD VS TEMPERATURE PHASE DIAGRAM

In this section, we conduct a study of the superconducting critical field vs temperature phase diagram of our twisted system. As mentioned previously, we consider a twist angle small enough for the system size to be of the order of the Moiré pattern unit cell (only a few unit cell are present at most), and we describe qualitatively the twisted system as a set of regions with different stacking, each of them with a particular band structure and with a particular DOS. If a superconducting phase is present in the twisted lattice, coupling of the superconducting order parameters in these regions should occur due to Josephson tunneling between them. This makes the study of the superconducting phase diagram in our twisted bilayer system particularly interesting due to the possible joint effect of several factors such as multiple bands, regions of different dimensionality, and DOS with van-Hove singularities. In particular, the experimental upper critical field curve

should reflect clearly the appearance of regions with different dimensionality as the twist angle increases (remaining small).

We can interpret qualitatively the twisted system as the n-band model, where each band is associated with one of the lattice regions with different orbital stackings. Depending on the position of the Fermi level, the analysis of the superconducting phase can be complex or simple depending on whether the Fermi level is in an energy range where the DOS of 2D and 1D regions overlap or not. In the latter case, superconductivity only involves the participation of the 2D regions or of the 1D regions which are effectively decoupled from each other since Josephson tunneling between them will be very small for small twist angles (again, if superconductivity occurs in the 2D regions, the 1D regions act as potential barriers). The superconducting critical field vs temperature phase diagram of 2D and quasi-1D superconductors has been described in the past both in the case of in-plane [43–49] and out-of-plane [38,49–53] magnetic field, and we know for instance that in the case of a quasi-1D system in transverse magnetic fields a dimensional crossover occurs at low temperature and the critical field diverges [39,54–56]. The effect of a van Hove singularity at the Fermi level or in its vicinity is somewhat similar leading to upward curvature in the critical field curve at low temperature [49,52,53].

In this section, we will address the more complex case with 2D and 1D regions DOS overlap at the Fermi level, such that more than one band participates in the formation of the superconducting state. Our analysis will be simplified assuming one band per region and interpreting the Josephson tunneling between 1D and 2D regions as interband pairing [57–59]. The upper critical field-vs-temperature phase diagrams H_{c2}-vs-T will be determined using the weak-coupling s-wave mean-field BCS approach (and using the usual eikonal treatment for coupled bands [60]). This method has been applied in the past by several authors when VHSs are present in the DOS at the Fermi level as well as in the case of a flat-band singularity at the Fermi level [21,61–63]. In addition, our approach is justified since we chose to broaden the flat bands in our upper critical field calculations in order to take into account the neglected hopping terms in our model and therefore a weak electron-phonon coupling limit is always possible (in contrast, one could argue that the presence of a nonbroadened flat band makes any interaction a strong one). Furthermore, we emphasize that the superconducting phase diagrams obtained in this paper would remain qualitatively the same even when assuming strong electron-phonon interactions, as in the case of the Eliashberg approach, since the main modifications in these diagrams result from the proximity to a dimensional crossover (due to the 1D bands) or density of states peaks and the effect of the latter is qualitatively the same whatever the approach. We opt to use the standard weak-coupling s-wave treatment as this is the simplest case where twisting effects can be addressed. Other pairing symmetries could be considered such as d-wave, but the main goal of our paper is to describe the twisting effects on a superconducting bilayer quasi-1D system and not the effects of the pairing symmetry.

We discuss in particular how the form of the normalized $[H_{c2}/H_{c2}(T=0)]$-vs-$[T/T_c(H=0)]$ curves changes with varying ratio between the intraband pairing interactions (this normalized upper critical field has a universal shape for 2D systems with constant DOS when magnetic field is applied perpendicular to the layers). Analyzing Figs. 5 and 6, we conclude that many different situations may occur depending on the position of the Fermi level. We limit our study to two simple situations: (i) a 2D band (associated with a 2D region) with constant DOS weakly coupled with a quasi-1D band (associated with a 1D region); (ii) a 2D band weakly coupled with a band with a van-Hove singularity. In this second case, the van-Hove singularity may be 1D-like or 2D-like. Nevertheless, we will adopt the approach of Refs. [49,52,53] and consider an isotropic 2D band with a van-Hove singularity that mimics the van-Hove singularity 1D-like exponent or the 2D-like exponent. These two cases are enough to show that the upper critical field curve can be used as a probe of twist angle applied to the bilayer system.

To determine H_{c2}, one needs to solve the two-band superconducting gap equations [60] which can be discretized as described in Appendix D,

$$\Delta_i^a = g\left[V^a \sum_j K_{ij}^a \Delta_j^a + V^{ab} \sum_j K_{ij}^b \Delta_j^b\right] \tag{13}$$

and

$$\Delta_i^b = g\left[V^b \sum_j K_{ij}^b \Delta_j^b + V^{ab} \sum_j K_{ij}^a \Delta_j^a\right], \tag{14}$$

where gV^a and gV^b are, respectively, the intraband pairing interactions in bands a and b, and gV^{ab} is the interband pairing interaction between those bands. $K_{ij}^a(K_{ij}^b)$ and $\Delta_j^a(\Delta_j^b)$ are the pair propagator and the gap function of the band $a(b)$. The factor g is an arbitrary constant that was introduced in order to interpret the previous equations as an eigenvalue equation [see Eq. (15)]. In this work, we did not attempt to find the dependence of the pairing interactions on the twist angle. One may argue that the interband pairing which reflects the Josephson tunneling between different regions should increase as the twist angle increases (while the "intraregion" pairing interaction should remain more or less the same in the case of the region corresponding to the untwisted stacking) reflecting the increase of the portion of the Moiré pattern corresponding to the surface between the different regions.

Equations (13) and (14) can be written as a single vector equation

$$\begin{bmatrix}\Delta_i^a \\ \Delta_i^b\end{bmatrix} = gM\begin{bmatrix}\Delta_j^a \\ \Delta_j^b\end{bmatrix}, \tag{15}$$

where

$$M = \begin{bmatrix}V^a K^a & V^{ab} K^b \\ V^{ab} K^a & V^b K^b\end{bmatrix}, \tag{16}$$

and the upper critical field is obtained from the highest eigenvalue of the matrix M, which can be achieved by, for instance, applying the Lanczos method. In Appendix B, we derive the n-band gap equation and the pair propagators for each band. In Appendix C, we introduce the n-band gap equation in a mixed representation (useful to work with anisotropic pair propagators) and in Appendix D, we describe the Lanczos method used to solve the gap equations.

Next, we ascertain the role of the quasi-1D and the van-Hove bands in the form of the upper critical field curve for

the two-band models, considering different ratios between the intraband pairings of those bands and the 2D band. (i) In the first case, we consider an isotropic 2D band with an energy-band dispersion $\epsilon_k = v_F(k - k_F)$, where v_F is the Fermi velocity and k_F is the Fermi momentum. The DOS of this band overlaps with the DOS of a band of a quasi-1D superconductor, with an energy-band dispersion $\epsilon_k - \mu = v_F(|k_x| - k_F) - 2t_y \cos(k_y)$, where t_y is very small [reflecting the weak hopping terms in the 1D regions that were neglected due to the condition Eq. (11)], and k_x and k_y are, respectively, the momentum in the direction x and y. (ii) In the second case, the 2D band DOS overlaps with the DOS of a band with a van-Hove singularity. In order to remove the effect of dimensionality, which is addressed in the previous case, we follow the approach of Refs. [49,52,53] and adopt the isotropic dispersion relation $\epsilon_k - \epsilon_{vh} = a \times sign(q)|q|^b$, where $q = k - k_{vh}$, ϵ_{vh} and k_{vh} are, respectively, the energy and momentum at the van-Hove singularity respective to the flat band, and a and b are constant parameters that control the extension of the saddle point.

In Fig. 8(a), the H_{c2}-vs-T phase diagrams are shown for the first case when the intraband interactions ratio is $V^{\sim 1D}/V^{2D} = 8, 9, 10, 11$, and the weak interband pairing interaction is given by $V^{\sim 1D,2D}/V^{2D} = 0.05$ where V^{2D} is the intraband interaction of the 2D band, and $V^{\sim 1D}$ is the intraband interaction of the quasi-1D band. For $V^{\sim 1D}/V^{2D} = 8$ (red curve), the phase diagram is still typical of a 2D conventional superconductor. The upper critical field is maximum for $T = 0$ and decreases with T as a parabola (negative curvature), reaching zero at a critical temperature T_c. For $V^{\sim 1D}/V^{2D} = 9$ (brown curve), at low temperatures, the curvature becomes positive, with the field diverging at a finite low temperature. As one increases $V^{\sim 1D}$, this behavior extends to intermediate temperatures ($V^{\sim 1D}/V^{2D} = 10$, green curve), and for large enough $V^{\sim 1D}$ it occurs at temperatures close to the critical temperature ($V^{\sim 1D}/V^{2D} = 11$, blue curve).

The phase diagrams for the second case are shown in Fig. 4, for $V^{vh}/V^{2D} = 0.5, 1.5, 2.0$, $V^{vh,2D}/V^{2D} = 0.05$, $a = 1$, and $b = 3$, where V^{vh} is the intraband pairing interaction for the band with a van-Hove singularity, and $V^{vh,2D}$ is the interband pairing interaction. For $V^{vh}/V^{2D} = 0.5$ (red curve), the phase diagram obtained is very close to the one of a typical 2D conventional superconductor, but at low temperatures we start to see a positive curvature on the critical field curve. This behavior becomes more obvious for $V^{vh}/V^{2D} = 1.5$ (brown curve) and starts to happen at higher temperatures as one increases V^{vh}/V^{2D}, as one can see in the case where $V^{vh}/V^{2D} = 2.0$ (green curve). By continually increasing V^{vh}/V^{2D}, the curvature of the critical field curve eventually becomes positive in the whole range of temperatures. In that case, the phase diagram obtained is close to that of a one-band superconductor with a band with a van-Hove singularity and as such, at low temperatures, the field decreases with temperature as a power law.

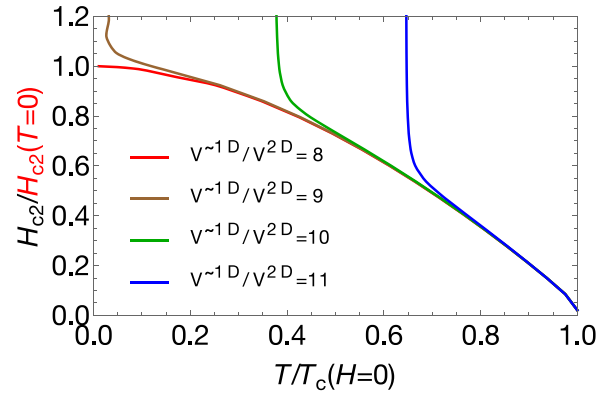

(a)

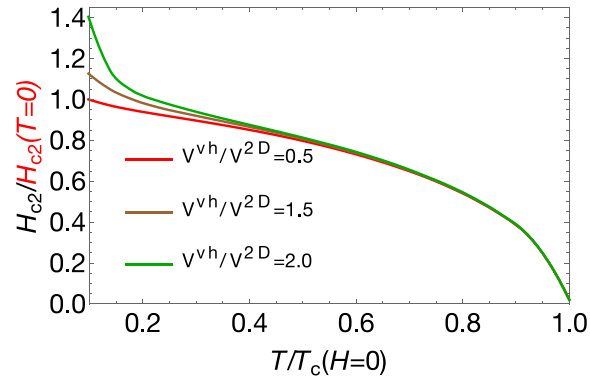

(b)

FIG. 8. Critical field vs temperature phase diagram of a two-band model (a) with a quasi-1D band and a 2D band; (b) with a band with a van-Hove singularity and a 2D band. In (a), the phase diagrams are plotted for the following values of the intraband interactions ratio $V^{\sim 1D}/V^{2D} = 8, 9, 10, 11$, assuming $K_F{}^{2D} = 1$, $v_F{}^{2D} = 1$, and $t_y/v_F{}^{\sim 1D} = 1.625$. The interband interaction is kept fixed, $V^{\sim 1D,2D}/V^{2D} = 0.05$. In (b) the diagrams obtained are for $V^{vh}/V^{2D} = 0.5, 1.5, 2.0$, assuming $K_F{}^{2D} = 1$, $v_F{}^{2D} = 1$, $K_F{}^{vh} = 1$, and the parameters $a = 1$, $b = 3$. The interband interaction is also in this case kept fixed, with $V^{vh,2D}/V^{2D} = 0.05$.

VII. CONCLUSION

The large interest in twisted bilayer systems in recent years has been motivated by the experimental finding of the superconducting phase in twisted bilayer graphene. These states are absent in single graphene sheets and are very similar to those seen in copper-oxide-based high-T_c superconductors [3]. This phase occurs at certain magic twist angles reflecting the flattening of particular bands near the Fermi level.

In this paper, we consider a different scenario where a nearly flat band is already present in a bilayer system with a 90° twist that resembles a Mielke lattice. This system consists of a stack of two identical quasi-1D layers, with each quasi-1D layer composed of a set of chains with p-wave orbitals at each site aligned with the direction of the chain. Calculating the hopping integrals using the Slater-Koster method, if we introduce a threshold in the hopping integrals larger than the transverse hopping integral between chains in the same layer, an exactly flat band is found at a particular interlayer distance (that should be accessible applying an uniaxial pressure). The presence of a twist in this system is particularly interesting since 1D or 2D regions appear in the Moiré pattern. We have characterized these regions according to stacking, band structure, and DOS. The same analysis was carried for an

untwisted bilayer system. This system can be classified as a Creutz ladderlike lattice, and it also has a nearly flat band for the interlayer spacing that generates the flat band in the Mielke-like lattice. The contrasting feature when comparing with the previous case is that this untwisted system is 1D and only introducing a twist we find 2D regions in the Moiré pattern (it is opposite in the case of the Mielke-like bilayer system).

The possibility of a superconducting phase in these systems was addressed using a qualitative approach that relies on the interpretation of the twisted bilayer lattice as a n-band model, where each band is associated to a particular region of the lattice. This approach is proposed in the case of system sizes of the order of the Moiré pattern unit cell (corresponding to small twist angles), where methods relying on Moiré Bloch bands are not useful. Josephson tunneling between different regions is interpreted as interband pairing interactions [57–59]. An additional approximation was to reduce this n-band system to a two band system with one of the bands describing a 2D region and the other corresponding to a quasi-1D region or a region with a van-Hove singularity. Our objective was to show in particular that the upper critical field transition curve was sensitive to the twist angle as expected. In the first case, we find that the critical field curve behaves closely to what is expected of a 2D superconductor if the intraband pairing interaction of the quasi-1D band is small. Though, for intermediate values of this pairing interaction, the parabolic behavior at low temperatures changes, and the critical curve gains positive curvature, diverging at a finite low temperature. This behavior is extended to temperatures close to the critical temperature for large quasi-1D bandwidths. In the second case, the critical field curve gains positive curvature at low temperatures for small values of the intraband interaction of the band with a van-Hove singularity, and this behavior starts to happen at higher temperatures for larger intraband values. For large enough intraband interaction, this behavior is extended to the whole temperature range.

Some results similar to those discussed in this paper were proposed in *ab initio* simulations of twisted bilayer GeSe [64]. In this reference, a crossover from an effectively 1D to a 2D system is also reported as the twist angle is increased. However, the flat bands reported in this reference are dispersive in one spatial direction and therefore they are not flat bands in the interpretation followed in our paper (no dispersion in any direction). Nevertheless, this reference shows that in more realist simulations of the quasi-1D bilayer materials, qualitative features discussed in this paper such as the competition between 1D and 2D regions in the twisted system are also found. On that note, our analysis of the critical field vs temperature phase diagram should be relevant to other twisted bilayer systems with flat bands if the following underlying assumptions also occur: (i) multiple-band superconductivity (2D band overlapping with a quasi-1D band at the Fermi level or with a band with a van-Hove singularity); (ii) system sizes smaller or of the order of the Moiré pattern unit cell. However, for instance, this is not the usual situation for the twist angles that generate superconductivity in TBG, which generate an isolated flat band at the Fermi level and where large system sizes are considered that justify the consideration of Moiré bands [13].

Notice that flat-band superconductivity may not always be fully captured by the standard weak-coupling s-wave treatment used in our study, and strong electron-electron interactions (which, for instance, in TBG leads to drastic modifications on the band structure giving rise to band flattening [22,23]) may need to be considered. The effect of such interactions could, however, be qualitatively incorporated in our BCS approach by using a modified DOS with stronger VHSs since these are strengthened by such interactions (as suggested in the extended van-Hove scenario for the high-T_c superconductors [65]), and that would make the low temperature curvature of the upper critical field curve more pronounced [53].

Finally, we would like to point out that our lattice can be generalized replacing each site by, for instance, a four-site ring which admits as eigenstates an s-orbital state ($k_{\text{ring}} = 0$), p_x and p_y states (symmetric and antisymmetric combinations of the $k_{\text{ring}} = \pm\pi/2$ states), and a $d_{x^2-y^2}$-orbital state ($k_{\text{ring}} = \pi$). The chains of these rings naturally form bands associated with each orbital and one can more easily envisage a geometry where the hoppings between different chains in the same layer can be neglected.

ACKNOWLEDGMENTS

This work is funded by the FEDER funds through the COMPETE 2020 Programme and National Funds through FCT - Portuguese Foundation for Science and Technology under the project UIDB/50025/2020 & UIDP/50025/2020 and under the project PTDC/FIS-MAC/29291/2017. F.D.R.S. acknowledges the financial support from the Portuguese Science and Technology Foundation (FCT) through the Grant BI 42 (27694/2019).

APPENDIX A: DECOMPOSITION OF ROTATED p_y ORBITALS

When a rotation is applied to the p_y orbitals of layer 2, the wave functions that describe such orbitals gain a component in the x direction, and thus one can no longer use Eq. (6) to determine the interlayer hopping energies. Nonetheless, the rotated orbitals can be decomposed into a combination of p_x and p_y orbitals, and those hopping energies can be obtained by combining Eqs. (1) and (6).

We can relate the rotated orbital $|p_{y'}\rangle$ with the original p_y orbital $|p_y\rangle$ by

$$|p_{y'}\rangle = \hat{R}_z(\theta_t)\,|p_y\rangle\,, \tag{A1}$$

with the rotation operator in z (remember that the rotation axis is transversal to the system) being given by $\hat{R}_z(\theta_t) = e^{-i\theta_t \hat{L}_z/\hbar}$, where the angular momentum operator $\hat{L}_z$ in the subspace $l = 1, m = 1, 0, 1$, is given by

$$\hat{L}_z = \hbar \begin{bmatrix} 1 & 0 & 0 \\ 0 & 0 & 0 \\ 0 & 0 & -1 \end{bmatrix}. \tag{A2}$$

Since p_y and p_x orbitals are given, respectively, by

$$\psi_{np_y} = -\frac{1}{\sqrt{2}}[\psi_{n,1,1} - \psi_{n,1,-1}] \Rightarrow |p_y\rangle$$
$$= -\frac{1}{\sqrt{2}}(|m=1\rangle - |m=-1\rangle), \quad \text{(A3)}$$
$$\psi_{np_x} = \frac{i}{\sqrt{2}}[\psi_{n,1,1} + \psi_{n,1,-1}] \Rightarrow |p_x\rangle$$
$$= \frac{i}{\sqrt{2}}(|m=1\rangle + |m=-1\rangle), \quad \text{(A4)}$$

we may write the matrix representation of the rotation operator in the subspace $|m=\pm 1\rangle$

$$R_z(\hat{\theta}_t) = \begin{bmatrix} e^{-i\theta_t} & 0 \\ 0 & e^{i\theta_t} \end{bmatrix}, \quad \text{(A5)}$$

and, in this basis, $|p_y\rangle$ and $|p_x\rangle$ are written as

$$|p_y\rangle = -\frac{1}{\sqrt{2}}\begin{bmatrix} 1 \\ -1 \end{bmatrix}, \quad \text{(A6)}$$
$$|p_x\rangle = \frac{i}{\sqrt{2}}\begin{bmatrix} 1 \\ 1 \end{bmatrix}. \quad \text{(A7)}$$

Finally, applying Eq. (A5) to Eq. (A6) we obtain the following expression

$$\hat{R}_z(\theta)\,|p_y\rangle = \cos\theta_t\,|p_y\rangle + \sin\theta_t\,|p_x\rangle\,, \quad \text{(A8)}$$

and thus, the interlayer hopping energies can be determined by

$$V_{xy'} = \cos(\theta_t)V_{xy} + \sin(\theta_t)V_{xx}. \quad \text{(A9)}$$

APPENDIX B: *n*-BAND GAP EQUATION AND PAIR PROPAGATORS

1. *n*-band gap equation

The Hamiltonian for a n-band 2D superconductor under perpendicular magnetic fields is given by [60]

$$H = H_i + H_{\text{int}}, \quad \text{(B1)}$$

with

$$H_i = \sum_i \left\{ -\frac{1}{2m_i}\sum_\sigma \int \Psi^\dagger_{i\sigma}(\mathbf{r})[\nabla - ieA(\mathbf{r})]^2\Psi_{i\sigma}(\mathbf{r})d\mathbf{r} \right.$$
$$\left. - V_{ii}\int \Psi^\dagger_{i\uparrow}(\mathbf{r})\Psi^\dagger_{i\downarrow}(\mathbf{r})\Psi_{i\downarrow}(\mathbf{r})\Psi_{i\uparrow}(\mathbf{r})d\mathbf{r} \right\}, \quad \text{(B2)}$$

and

$$H_{\text{int}} = \sum_{i\neq j}\left[-V_{ij}\int \Psi^\dagger_{i\uparrow}(\mathbf{r})\Psi^\dagger_{i\downarrow}(\mathbf{r})\Psi_{j\downarrow}(\mathbf{r})\Psi_{j\uparrow}(\mathbf{r})d\mathbf{r} + \text{H.c.}\right], \quad \text{(B3)}$$

where i, j label the bands, m_i is the mass of i-band electrons, and $\Psi^\dagger_{i\sigma}(\mathbf{r})(\Psi_{i\sigma}(\mathbf{r}))$ creates (annihilates) a i-band electron with spin σ and charge e at position $\mathbf{r}$. V_{ii} and V_{ij} are, respectively, the intraband and interband pairing interactions and $A(\mathbf{r})$ is the magnetic vector potential.

From Eq. (B1), in the case of a one-band system, one obtains the usual differential equations for the Green's functions in real space, defined in Refs. [66,67], and these equations remain unchanged in the case of a n-band system [60] (with a generalized expression for the gap functions) and are given by

$$\left(i\omega + \frac{1}{2m_i}[\nabla_r - ie\mathbf{A}(\mathbf{r})]^2 + \mu_i\right)\mathscr{G}^{HS}_{i,\omega}(\mathbf{r},\mathbf{r}')$$
$$+ \int d\tilde{\mathbf{r}}\Delta_i(\mathbf{r},\tilde{\mathbf{r}})\mathscr{F}^\dagger_{i,\omega}(\tilde{\mathbf{r}},\mathbf{r}') = \delta(\mathbf{r}-\mathbf{r}'), \quad \text{(B4)}$$

and

$$\left(-i\omega + \frac{1}{2m_i}[\nabla_r + ie\mathbf{A}(\mathbf{r})]^2 + \mu_i\right)\mathscr{F}^\dagger_{i,\omega}(\mathbf{r},\mathbf{r}')$$
$$- \int d\tilde{\mathbf{r}}\Delta^*_i(\mathbf{r},\tilde{\mathbf{r}})\mathscr{G}^{HS}_{i,\omega}(\tilde{\mathbf{r}},\mathbf{r}') = 0, \quad \text{(B5)}$$

where the Green's function $\mathscr{G}^{HS}_{i,\omega}$ describes the superconducting state in a magnetic field $\mathscr{F}^\dagger_{i,\omega}$ is the anomalous Green's function, and the n-band energy gap Δ_i is given by [60]

$$\Delta^*_i(\mathbf{r},\mathbf{r}) = k_BT\left[V_{ii}\mathscr{F}^\dagger_{i,\omega}(\mathbf{r},\mathbf{r}) + \sum_{j\neq i}V_{ij}\mathscr{F}^\dagger_{j,\omega}(\mathbf{r},\mathbf{r})\right]. \quad \text{(B6)}$$

In order to derive the n-band gap equation, one may follow the following steps, laid out in the works [39,60]. The normal state Green's function $\mathscr{G}^H_{i,\omega}$ satisfies the following equation

$$\left(i\omega + \frac{1}{2m_i}[\nabla_{r'} + ie\mathbf{A}(\mathbf{r}')]^2 + \mu\right)\mathscr{G}^H_{i,\omega}(\mathbf{r},\mathbf{r}') = \delta(\mathbf{r}-\mathbf{r}'), \quad \text{(B7)}$$

which can be used to rewrite Eqs. (B4) and (B5) into

$$\mathscr{G}^{HS}_{i,\omega}(\mathbf{r},\mathbf{r}') = \mathscr{G}^H_{i,\omega}(\mathbf{r},\mathbf{r}') - \int d\tilde{\mathbf{r}}d\mathbf{l}\mathscr{G}^H_{i,\omega}(\mathbf{r},\mathbf{l})\Delta_i(\mathbf{l},\tilde{\mathbf{r}})\mathscr{F}^\dagger_{i,\omega}(\tilde{\mathbf{r}},\mathbf{r}'), \quad \text{(B8)}$$

and

$$\mathscr{F}^\dagger_{i,\omega}(\mathbf{r},\mathbf{r}') = \int d\tilde{\mathbf{r}}d\mathbf{l}\mathscr{G}^H_{i,-\omega}(\mathbf{l},\mathbf{r})\Delta^*_i(\mathbf{l},\tilde{\mathbf{r}})\mathscr{G}^{HS}_{i,\omega}(\tilde{\mathbf{r}},\mathbf{r}'). \quad \text{(B9)}$$

Since the energy gap is very small in the vicinity of the upper critical transition curve, one can expand $\mathscr{F}^\dagger_{i,\omega}(\mathbf{r},\mathbf{r})$ in powers of Δ. In order to obtain the band gap equation, one linearizes Eq. (B9), replace $\mathscr{G}^{HS}_{i,\omega}$ by $\mathscr{G}^H_{i,\omega}$, and substitutes it in Eq. (B6). Note that in the absence of magnetic field, the gap function only depends on the relative position of the pair, i.e., $\Delta(\mathbf{r},\mathbf{r}') \to \Delta(\mathbf{r}-\mathbf{r}')$. In the particular case of a local pairing interaction, $V(\mathbf{r}-\mathbf{r}') = V\delta(\mathbf{r}-\mathbf{r}')$, one obtains the usual s-wave gap function, $\Delta(\mathbf{r},\mathbf{r}') = \Delta\delta(\mathbf{r}-\mathbf{r}')$. In the presence of a magnetic field it comes that

$$\Delta(\mathbf{r},\mathbf{r}') = \Delta(\mathbf{r})\delta(\mathbf{r}-\mathbf{r}'), \quad \text{(B10)}$$

and the band gap equation becomes

$$\Delta_i(\mathbf{r}) = V_{ii}\int d\mathbf{r}'K^H_{\beta i}(\mathbf{r}',\mathbf{r})\Delta_i(\mathbf{r}')$$
$$+ \sum_{j\neq i}V_{ij}\int d\mathbf{r}'K^H_{\beta j}(\mathbf{r}',\mathbf{r})\Delta_j(\mathbf{r}'), \quad \text{(B11)}$$

with $i = 1, ..., n$, and where $K^H_{\beta i}(\mathbf{r}',\mathbf{r})$ is the pair propagator defined by

$$K^H_{\beta i}(\mathbf{r}',\mathbf{r}) = \frac{1}{\beta}\sum_\omega \mathscr{G}^H_{i,-\omega}(\mathbf{r}',\mathbf{r})\mathscr{G}^H_{i\omega}(\mathbf{r}',\mathbf{r}). \quad \text{(B12)}$$

Under the semiclassic approximation (for not high enough magnetic fields, the effects resulting from these fields can be included into the electronic behavior in a semiclassic way) [66–68] one has

$$K^H_{\beta i}(\mathbf{r}', \mathbf{r}) = K_{\beta i}(\mathbf{r}' - \mathbf{r}) e^{(i\frac{2e}{\hbar c}\mathbf{A}(\mathbf{r}).(\mathbf{r}'-\mathbf{r}))}, \tag{B13}$$

where $K_{\beta i}(\mathbf{r})$ is the fermion pair propagator in real space at a temperature $k_B T = 1/\beta$, in the absence of external fields, intraband, and interband pairing interactions. The superconducting transition for a 2D system in an external magnetic field can then be described by the following semiclassical linearized n-band gap equation

$$\Delta_i(\mathbf{r}) = V_{ii} \int d\mathbf{r}' K_{\beta i}(\mathbf{r}') e^{i2\mathbf{A}(\mathbf{r}).(\mathbf{r}'-\mathbf{r})} \Delta_i(\mathbf{r}+\mathbf{r}') + \sum_{j\neq i} V_{ij} \int d\mathbf{r}' K_{\beta j}(\mathbf{r}') e^{i2\mathbf{A}(\mathbf{r}).(\mathbf{r}'-\mathbf{r})} \Delta_j(\mathbf{r}+\mathbf{r}'), \tag{B14}$$

where the geometrized unit system, i.e., $\hbar = c = e = k_B = \mu_B = 1$, was used.

In the 2D symmetric gauge $\mathbf{A} = \frac{1}{2}\mathbf{H} \times \mathbf{r}$, Eq. (B14) becomes

$$\Delta_i(\mathbf{r}) = V_{ii} \int d\mathbf{r}' K_{\beta i}(\mathbf{r}') e^{i\frac{\mathbf{r}\times\mathbf{r}'}{l^2}} \Delta_i(\mathbf{r}+\mathbf{r}') + \sum_{j} V_{ij} \int d\mathbf{r}' K_{\beta j}(\mathbf{r}') e^{i\frac{\mathbf{r}\times\mathbf{r}'}{l^2}} \Delta_j(\mathbf{r}+\mathbf{r}'), \tag{B15}$$

where l is related to the magnetic field by $H = \phi_0(2\pi l^2)^{-1}$, with $\phi_0 = hc/e$ being the flux quantum. The highest eigenvalue of this linear equation determines the upper critical field.

2. Pair propagator for an isotropic 2D conventional superconductor

The retarded Green's function for an isotropic 2D conventional superconductor, with energy-band dispersion $\epsilon_k - \mu = v_F(k - k_F)$, is given by

$$G^R(k, \omega) = \frac{1}{\omega - v_F(k - k_F) + i0^+}, \tag{B16}$$

where ω is the frequency energy. The spectral function, in the real space, is given by the following [39]

$$A(r, \omega) = -\frac{1}{2v_F}\left(\frac{\omega}{k_F} + k_F\right) J_0\left[r\left(\frac{\omega}{k_F} + k_F\right)\right]\theta(\omega + v_F k_F) \approx -\frac{1}{4v_F}\sqrt{\frac{2k_F}{\pi r}} \cos\left[r\left(\frac{\omega}{k_F} + k_F\right) - \frac{\pi}{4}\right], \tag{B17}$$

where J_0 is the Bessel function $J_n(x)$ for $n = 0$. After some math, and using Eq. (B12), one obtains the pair propagator for an isotropic 2D conventional superconductor

$$K_\beta(r) = \left(\frac{k_F}{2\pi r}\right)^{-1} \frac{1}{v_F^2 \beta} \frac{1}{\sinh\left(\frac{2\pi r}{\beta v_F}\right)}. \tag{B18}$$

3. Pair propagator for a high-density quasi-1D superconductor

The energy-band dispersion for an anisotropic high-density quasi-1D superconductor is given by

$$\epsilon_k - \mu = v_F(|k_x| - k_F) - 2t_y \cos(k_y), \tag{B19}$$

which is associated to an open Fermi surface (for $t_y = 0$ one recovers the expression for the isotropic 2D conventional superconductor). The retarded Green's function is then given by [39]

$$G^R(k, \omega) = \frac{1}{\omega - v_F(|k_x| - k_F) - 2t_y \cos(k_y)}, \tag{B20}$$

and the real spectral function by

$$A(\omega, x, y) = A^{1D}(\omega, x) e^{-iy\pi/2}, \tag{B21}$$

where $-A^{1D}(\omega, x)/\pi$ is the spectral function of the noninteracting 1D Tomonaga model

$$A^{1D}(\omega, x) = -\frac{1}{v_F} \cos\left[\left(\frac{\omega}{v_F} + k_F\right)x\right]. \tag{B22}$$

The corresponding pair propagator is given by

$$K_\beta(x) = K^{1D}_\beta(x, y) J_y^2\left[\frac{2t_y x}{v_F}\right], \tag{B23}$$

where

$$K^{1D}_\beta(x, y) = \frac{1}{v_F^2 \beta} \frac{1}{\sinh\left[\frac{2\pi r}{\beta v_F}\right]}. \tag{B24}$$

4. Pair propagator for a superconductor with an isotropic band with a van-Hove singularity

The energy-band dispersion for an isotropic band with a van-Hove singularity (with the vHS being pinned at the Fermi level) is given by $\epsilon_k - \epsilon_{vh} = a \times \text{sign}(q)|q|^b$. In this case, the retarded Green's function is the following

$$G^R(k, \omega) = \frac{1}{\omega - a \times \text{sign}(q)|q|^b}, \tag{B25}$$

and the spectral function is given by [49,52,53]

$$A(r, \omega) = -\frac{1}{2ab}\left(\frac{|\omega|}{a}\right)^{(1/b)-1} \times \sqrt{\frac{2k_F}{\pi r}} \times \cos\left[r\left(\left(\frac{|\omega|}{a}\right)^{1/b} \text{sign}\,\omega + k_F\right) - \frac{\pi}{4}\right], \tag{B26}$$

where a and b are constant parameters that control the extension of the saddle point. The corresponding pair propagator is given by

$$K_\beta(r) = r^{(b-3)} F\left[\left(\frac{\beta a}{2}\right)^{1/b}/r\right], \tag{B27}$$

with

$$F[X] = \frac{2k_F}{\pi^2}\frac{1}{ab}\int_0^\infty d\omega \frac{\tanh\left[(\omega X)^b\right]}{\omega^{b-1}} \left\{\frac{1}{2}\sin(2\omega) + \sum_{n=1}^{\frac{b-1}{2}} e^{-\omega \sin(2\pi/b_n)} \times \sin\left[\omega\left(1 + \cos\left(\frac{2\pi}{b}n\right)\right) + \frac{2\pi}{b}n\right]\right\}. \tag{B28}$$

APPENDIX C: BAND GAP EQUATION IN THE MIXED REPRESENTATION AND DEGENERACY OF THE GAP SOLUTIONS

Band gap equation in the mixed representation

In this section we derive the n-band gap equation in the mixed representation. We generalize the gap equation in Ref. [39] for the case of n bands. We use this representation due to the anisotropic nature of the pair propagator given in Eq. (B23). In such a case, it is easier to find the numerical solutions of the gap equations by including the effects of the magnetic field as a phase term $e^{i(\mathbf{A}(\mathbf{r})+\mathbf{A}(\mathbf{r}'))}$, due to the symmetric form of those phases. In the case of the Landau gauge $A = (0, H_x, 0)$, the pair propagator can be written as

$$K^H_{\beta i}(\mathbf{r}', \mathbf{r}) = K_{\beta i}(\mathbf{r}' - \mathbf{r})e^{iH(x+x')(y'-y)}, \tag{C1}$$

and the gap equation (B15) becomes

$$\begin{aligned}\Delta_i(x, y) = V_{ii} \int dx' \int dy' K_{\beta i}(x' - x, y' - y)e^{iH(x+x')(y'-y)}\Delta_i(x', y') \\ + \sum_{i\neq j} V_{ij} \int dx' \int dy' K_{\beta j}(x' - x, y' - y)e^{iH(x+x')(y'-y)}\Delta_j(x', y'),\end{aligned} \tag{C2}$$

or, upon the variable change $x' - x = x'$,

$$\begin{aligned}\Delta_i(x, y) = V_{ii} \int dx' \int dy' K_{\beta i}(x', y')e^{iH(2x+x')y'}\Delta_i(x + x', y + y') \\ + \sum_{i\neq j} V_{ij} \int dx' \int dy' K_{\beta j}(x', y')e^{iH(2x+x')y'}\Delta_j(x' + x', y + y').\end{aligned} \tag{C3}$$

By using the Fourier transformation in y and noting that

$$\frac{1}{\sqrt{2\pi}} \int dy \Delta_i(x + x', y + y')e^{-ik_y y} = \frac{1}{\sqrt{2\pi}} \int dy \Delta_i(x + x', y)e^{-ik_y(y-y')} = e^{ik_y y'}\Delta_i(x + x', k_y), \tag{C4}$$

we obtain the following

$$\begin{aligned}\Delta_i(x, k_y) = V_{ii} \int dy' \int dx' K_{\beta i}(x', y')e^{i(k_y+H(2x+x'))y'}\Delta_i(x + x', k_y) \\ + \sum_{i\neq j} V_{ij} \int dy' \int dx' K_{\beta j}(x', y')e^{i(k_y+H(2x+x'))y'}\Delta_j(x + x', k_y).\end{aligned} \tag{C5}$$

Using the proof of the degeneracy of $\Delta(x, ky)$ (this proof can be found for instance in Ref. [39]; note that in that proof, it was assumed that $\int_{\mathbf{r}}^{\mathbf{r}'} drA(\mathbf{r}) \equiv A(\mathbf{r})(\mathbf{r}' - \mathbf{r})$, but that should not matter), we obtain

$$\begin{aligned}\Delta_i(x, k_y = 0) = V_{ii} \int dx' K_{\beta,i}(x', k_y = -H(2x + x'))\Delta_i(x + x', k_y = 0) \\ + \sum_{i\neq j} V_{ij} \int dx' K_{\beta,j}(x', k_y = -H(2x + x'))\Delta_j(x + x', k_y = 0),\end{aligned} \tag{C6}$$

or equivalently

$$\begin{aligned}\Delta_i(x, 0) = V_{ii} \int dx' K_{\beta,i}(x' - x, k_y = -H(x + x'))\Delta_i(x', 0) \\ + \sum_{i\neq j} V_{ij} \int dx' K_{\beta,j}(x' - x, k_y = -H(x + x'))\Delta_j(x', 0),\end{aligned} \tag{C7}$$

where $\Delta_i(x, 0)$ is the y integrated gap function and $K_\beta(x, k_y)$ are the Fourier transforms of $K_\beta(x, y)$

$$K_\beta(x, k_y) \sim \int d\omega \int dp_y \tanh(\beta\omega/2)A(x, p_y + k_y, \omega)B(x, -p_y, -\omega), \tag{C8}$$

where

$$A(x, k_y, \omega) = \frac{1}{2\pi} \int dk_x e^{ik_x x} ImG^R(\boldsymbol{k}, \omega), \tag{C9}$$

and

$$B(x, k_y, \omega) = \frac{1}{2\pi} \int dk_x e^{ik_x x} ReG^R(\boldsymbol{k}, \omega). \tag{C10}$$

APPENDIX D: NUMERICAL LANCZOS SOLUTIONS OF THE GAP EQUATION

1. Discretization of the gap equation

The determination of the H_{c2} curve by analytically solving Eq. (C7) is a hard task to achieve. Instead, we transform the gap equation into a vector equation, making the determination of H_{c2} as simple as solving an eigenvalue problem. In order to do that, following the procedure in Refs. [38,39] (and generalizing it for the n-band system), we make a discretization of the gap equation in one of the directions transforming it in a vector equation. In that case, Eq. (C7) can be written as

$$(\Delta_i)_n = V_{ii}\sum_m (K_{\beta i})_{nm}(\Delta_i)_m + \sum_{i\neq j} V_{ij}\sum_p (K_{\beta i})_{np}(\Delta_i)_p, \tag{D1}$$

where the index n labels the discrete coordinates. In the case of a two-band system, the two-band-gap equation in the vectorial form is the following

$$\Delta_i^a = g\left[V^a\sum_j K_{ij}^a\Delta_j^a + V^{ab}\sum_j K_{ij}^b\Delta_j^b\right] \tag{D2}$$

$$\Delta_i^b = g\left[V^b\sum_j K_{ij}^b\Delta_j^b + V^{ab}\sum_j K_{ij}^a\Delta_j^a\right], \tag{D3}$$

where $gV^a(V^b)$ is the intraband pairing interaction in the band $a(b)$ and gV^{ab} is the interband pairing interaction. $K_{ij}^a(K_{ij}^b)$ and $\Delta_j^a(\Delta_j^b)$ are, respectively, the pair propagator and the gap function of the band $a(b)$.

We can write Eqs. (D2) and (D3) as a single vector equation

$$\begin{bmatrix}\Delta_i^a\\ \Delta_i^b\end{bmatrix} = gM_{ij}\begin{bmatrix}\Delta_j^a\\ \Delta_j^b\end{bmatrix}, \tag{D4}$$

where

$$M_{ij} = \begin{bmatrix}V^aK^a & V^{ab}K^b\\ V^{ab}K^a & V^bK^b\end{bmatrix}. \tag{D5}$$

In this case, the upper critical field is obtained from the highest eigenvalue of the matrix M_{ij}. This eigenvalue was obtained by applying the Lanczos method [39], and the respective eigenstate gives the gap function. The numerical determination of the highest eigenvalue of the matrix M_{ij} changes the gap equation to the following simple equation

$$0 = f(H_{c2}, T) - \frac{1}{g}, \tag{D6}$$

which can be solved by applying a secant method.

2. Lanczos method

The Lanczos method is a numerical algorithm suitable to determine, approximately, extreme eigenvalues and eigenvectors of large sparse matrices in a considerably lower time when compared to the direct diagonalization of the same matrices [69]. In this section, we present the Lanczos method following Ref. [69].

The states with the lowest energy are found by applying a step-descent algorithm to a generic initial state. The energy E of an eigenvector ψ of a matrix H is given by

$$E\,|\psi\rangle = H\,|\psi\rangle \Leftrightarrow E\,\langle\psi|\psi\rangle = \langle\psi|H|\psi\rangle \Leftrightarrow E = \frac{\langle\psi|H|\psi\rangle}{\langle\psi|\psi\rangle}, \tag{D7}$$

and this energy is minimized for $\psi = \psi_0$, with $E(\psi_0) = E_0$.

Step-descent:

$$\frac{\partial E[\psi]}{\langle\psi|} = \frac{H\,|\psi\rangle - E[\psi]\,|\psi\rangle}{\langle\psi|\psi\rangle} = |\psi\rangle_a \tag{D8}$$

with $E[\psi - \alpha\psi_a] < E[\psi]$, where a is a positive constant. We want to minimize $E[\psi - \alpha\psi_a]$, and that is equivalent to determining the lowest eigenvalue of the matrix formed by the orthogonal (and orthonormal) space spanned by the base vectors $|\psi\rangle$ and $|\psi_a\rangle$. In turn, that space is identical to the space spanned by the vectors $|\psi\rangle$ and $H\,|\psi\rangle$, i.e., span$(|\psi\rangle\,, |\psi_a\rangle)$ = span$(|\psi\rangle\,, H\,|\psi_a\rangle)$.

So, the first vector is $v_0 = \frac{|\psi\rangle}{\sqrt{\langle\psi\rangle}}$, and the second vector $|v_1\rangle$ is obtained by orthogonalizing $H\,|v_0\rangle$ to $|v_0\rangle$

$$|\tilde{v_1}\rangle = H\,|v_0\rangle - |v_0\rangle\,\langle v_0|H|v_0\rangle, \tag{D9}$$

and normalizing the resulting vector

$$|v_1\rangle = \frac{|\tilde{v_1}\rangle}{\sqrt{\langle\tilde{v_1}|\tilde{v_1}\rangle}} = \frac{|\tilde{v_1}\rangle}{b_1} \Leftrightarrow |\tilde{v_1}\rangle = b_1\,|v_1\rangle\,, \tag{D10}$$

where $b_1 = \sqrt{\langle\tilde{v_1}|\tilde{v_1}\rangle}$. We can rewrite Eq. (D9) as

$$H\,|v_0\rangle = a_0\,|v_0\rangle + |\tilde{v_1}\rangle \tag{D11}$$

or

$$H\,|v_0\rangle = a_0\,|v_0\rangle + b_1\,|v_1\rangle\,, \tag{D12}$$

where $a_n = \langle v_n|H|v_n\rangle$. Applying $\langle v_1|$ to Eq. (D12),

$$\langle v_1|H|v_0\rangle = b_1. \tag{D13}$$

Thus, the Hamiltonian in the base of vectors spanned by $|\psi\rangle$ and $H\,|\psi\rangle$, in the matricial form, is then given by

$$H_{v_0,v_1} = \begin{bmatrix}a_0 & b_1\\ b_1 & a_1\end{bmatrix}, \tag{D14}$$

and the lowest eigenvalue and the respective eigenstate of Eq. (D14) are given by

$$\lambda^- = \frac{(a_0+b_1) - \sqrt{{a_0}^2 + {b_1}^2 + 4{b_1}^2 - 2a_0b_1}}{2} \tag{D15}$$

and

$$v_{\lambda^-} = \left(-\frac{(-a_0+b_1) + \sqrt{{a_0}^2 + {b_1}^2 + 4{b_1}^2 - 2a_0b_1}}{2b_1}, 1\right). \tag{D16}$$

In our work, $H = M_{ij}$.

[1] A. H. MacDonald, Trend: Bilayer graphene's wicked, twisted road, Physics **12**, 12 (2019).

[2] Y. Cao, V. Fatemi, A. Demir, S. Fang, S. L. Tomarken, J. Y. Luo, J. D. Sanchez-Yamagishi, K. Watanabe, T. Taniguchi,

E. Kaxiras *et al.*, Correlated insulator behaviour at half-filling in magic-angle graphene superlattices, Nature (London) **556**, 80 (2018).

[3] Y. Cao, V. Fatemi, S. Fang, K. Watanabe, T. Taniguchi, E. Kaxiras, and P. Jarillo-Herrero, Unconventional superconductivity in magic-angle graphene superlattices, Nature (London) **556**, 43 (2018).

[4] A. Kerelsky, L. J. McGilly, D. M. Kennes, L. Xian, M. Yankowitz, S. Chen, K. Watanabe, T. Taniguchi, J. Hone, C. Dean *et al.*, Maximized electron interactions at the magic angle in twisted bilayer graphene, Nature (London) **572**, 95 (2019).

[5] Y. Choi, J. Kemmer, Y. Peng, A. Thomson, H. Arora, R. Polski, Y. Zhang, H. Ren, J. Alicea, G. Refael *et al.*, Electronic correlations in twisted bilayer graphene near the magic angle, Nat. Phys. **15**, 1174 (2019).

[6] E. Codecido, Q. Wang, R. Koester, S. Che, H. Tian, R. Lv, S. Tran, K. Watanabe, T. Taniguchi, F. Zhang *et al.*, Correlated insulating and superconducting states in twisted bilayer graphene below the magic angle, Sci. Adv. **5**, eaaw9770 (2019).

[7] K. Kim, A. DaSilva, S. Huang, B. Fallahazad, S. Larentis, T. Taniguchi, K. Watanabe, B. J. LeRoy, A. H. MacDonald, and E. Tutuc, Tunable moiré bands and strong correlations in small-twist-angle bilayer graphene, Proc. Natl. Acad. Sci. **114**, 3364 (2017).

[8] J. M. B. Lopes dos Santos, N. M. R. Peres, and A. H. C. Neto, Graphene Bilayer with a Twist: Electronic Structure, Phys. Rev. Lett. **99**, 256802 (2007).

[9] G. Trambly de Laissardière, D. Mayou, and L. Magaud, Localization of Dirac electrons in rotated graphene bilayers, Nano Lett. **10**, 804 (2010).

[10] S. Shallcross, S. Sharma, E. Kandelaki, and O. A. Pankratov, Electronic structure of turbostratic graphene, Phys. Rev. B **81**, 165105 (2010).

[11] M. N. Manaf, I. Santoso, and A. Hermanto, Density of states of Twisted bilayer graphene at Low Energy, in *Proceedings of the 2014 International Conference on Physics*, edited by I. Santoso, A. Kusumaatmaja, and F. Nugroho (Atlantis Press, Yogyakarta, 2014), Vol. 2.

[12] G. Li, A. Luican, J. M. B. Lopes dos Santos, A. H. C. Neto, A. Reina, J. Kong, and E. Y. Andrei, Observation of Van Hove singularities in twisted graphene layers, Nat. Phys. **6**, 109 (2010).

[13] R. Bistritzer and A. H. MacDonald, Moiré bands in twisted double-layer graphene, Proc. Natl. Acad. Sci. **108**, 12233 (2011).

[14] J. M. B. Lopes dos Santos, N. M. R. Peres, and A. H. C. Neto, Continuum model of the twisted graphene bilayer, Phys. Rev. B **86**, 155449 (2012).

[15] P. Moon and M. Koshino, Energy spectrum and quantum Hall effect in twisted bilayer graphene, Phys. Rev. B **85**, 195458 (2012).

[16] G. Tarnopolsky, A. J. Kruchkov, and A. Vishwanath, Origin of Magic Angles in Twisted Bilayer Graphene, Phys. Rev. Lett. **122**, 106405 (2019).

[17] E. S. Morell, J. D. Correa, P. Vargas, M. Pacheco, and Z. Barticevic, Flat bands in slightly twisted bilayer graphene: Tight-binding calculations, Phys. Rev. B **82**, 121407 (2010).

[18] M. Imada and M. Kohno, Superconductivity from Flat Dispersion Designed in Doped Mott Insulators, Phys. Rev. Lett. **84**, 143 (2000).

[19] S. Deng, A. Simon, and J. Köhler, A“ flat/steep band” model for superconductivity, Int. J. Mod. Phys. B **19**, 29 (2005).

[20] S. Miyahara, S. Kusuta, and N. Furukawa, BCS theory on a flat band lattice, Phys. C: Supercond. **460**, 1145 (2007).

[21] A. Julku, S. Peotta, T. I. Vanhala, D. Kim, and P. Törmä, Geometric Origin of Superfluidity in the Lieb-Lattice Flat Band, Phys. Rev. Lett. **117**, 045303 (2016).

[22] F. Guinea and N. R. Walet, Electrostatic effects, band distortions, and superconductivity in twisted graphene bilayers, Proc. Natl. Acad. Sci. **115**, 13174 (2018).

[23] Y. Choi, H. Kim, C. Lewandowski, Y. Peng, A. Thomson, R. Polski, Y. Zhang, K. Watanabe, T. Taniguchi, J. Alicea *et al.*, Interaction-driven band flattening and correlated phases in twisted bilayer graphene, arXiv:2102.02209.

[24] G. Shavit, E. Berg, A. Stern, and Y. Oreg, Theory of correlated insulators and superconductivity in twisted bilayer graphene, arXiv:2107.08486.

[25] W. Qin, B. Zou, and A. H. MacDonald, Critical magnetic fields and electron-pairing in magic-angle twisted bilayer graphene, arXiv:2102.10504.

[26] A. Mielke, Ferromagnetic ground states for the Hubbard model on line graphs, J. Phys. A **24**, L73 (1991).

[27] A. Mielke, Ferromagnetism in the Hubbard model on line graphs and further considerations, J. Phys. A **24**, 3311 (1991).

[28] A. Mielke, Exact ground states for the Hubbard model on the Kagome lattice, J. Phys. A **25**, 4335 (1992).

[29] H. Tasaki, Ferromagnetism in the Hubbard Models with Degenerate Single-Electron Ground States, Phys. Rev. Lett. **69**, 1608 (1992).

[30] A. Mielke and H. Tasaki, Ferromagnetism in the Hubbard model, Commun. Math. Phys. **158**, 341 (1993).

[31] O. Derzhko, J. Richter, and M. Maksymenko, Strongly correlated flat-band systems: The route from Heisenberg spins to Hubbard electrons, Int. J. Mod. Phys. A **29**, 1530007 (2015).

[32] F. D. R. Santos and R. G. Dias, Hole-localized states in interacting geometrically frustrated systems, Phys. Rev. B **99**, 125152 (2019).

[33] F. D. R. Santos and R. G. Dias, Methods for the construction of interacting many-body Hamiltonians with compact localized states in geometrically frustrated clusters, Sci. Rep. **10**, 4532 (2020).

[34] W. Li, W. Wu, and Z. Li, Controlling interlayer spacing of graphene oxide membranes by external pressure regulation, ACS Nano **12**, 9309 (2018).

[35] A. V. Talyzin, V. L. Solozhenko, O. O. Kurakevych, T. Szabó, I. Dékány, A. Kurnosov, and V. Dmitriev, Colossal pressure-induced lattice expansion of graphite oxide in the presence of water, Angew. Chem. **120**, 8392 (2008).

[36] P. Sun, R. Ma, H. Deng, Z. Song, Z. Zhen, K. Wang, T. Sasaki, Z. Xu, and H. Zhu, Intrinsic high water/ion selectivity of graphene oxide lamellar membranes in concentration gradient-driven diffusion, Chem. Sci. **7**, 6988 (2016).

[37] S. Carr, S. Fang, P. Jarillo-Herrero, and E. Kaxiras, Pressure dependence of the magic twist angle in graphene superlattices, Phys. Rev. B **98**, 085144 (2018).

[38] R. G. Dias and J. M. Wheatley, Superconducting upper critical field near a 2*D* van Hove singularity, Solid State Commun. **98**, 859 (1996).

[39] R. G. Dias, Anomalous correlations in low dimensional metals, Ph.D. thesis, University of Cambridge, 1996.

[40] J. C. Slater and G. F. Koster, Simplified LCAO method for the periodic potential problem, Phys. Rev. **94**, 1498 (1954).
[41] L. Goodwin, A. J. Skinner, and D. G. Pettifor, Generating transferable tight-binding parameters: Application to silicon, Europhys. Lett. **9**, 701 (1989).
[42] W. A. Harrison, Theory of the two-center bond, Phys. Rev. B **27**, 3592 (1983).
[43] H. Shimahara, Fulde-Ferrell state in quasi-two-dimensional superconductors, Phys. Rev. B **50**, 12760 (1994).
[44] R. G. Dias, Zeeman splitting in multiple-band superconductors, Phys. Rev. B **72**, 012505 (2005).
[45] R. G. Dias and J. A. Silva, Huge metastability in high-T_c superconductors induced by parallel magnetic field, Phys. Rev. B **67**, 092511 (2003).
[46] F. D. R. Santos, A. M. Marques, and R. G. Dias, Pauli limiting and metastability regions of superconducting graphene and intercalated graphite superconductors, Phys. Rev. B **93**, 045412 (2016).
[47] A. M. Marques, R. G. Dias, M. A. N. Araújo, and F. D. R. Santos, In-plane magnetic field versus temperature phase diagram of a quasi-2*D* frustrated multiband superconductor, Supercond. Sci. Technol. **28**, 045021 (2015).
[48] R. G. Dias and A. M. Marques, Frustrated multiband superconductivity, Supercond. Sci. Technol. **24**, 085009 (2011).
[49] R. G. Dias, Critical magnetic fields in superconductors with singular density of states, in *Strongly Correlated Systems, Coherence And Entanglement*, edited by J. M. P. Carmelo, J. M. B. Lopes dos Santos, V. Rocha Vieira, and P. D. Sacramento (World Scientific, Singapore, 2007), p. 421.
[50] R. G. Dias, A. J. Schofield, and J. M. Wheatley, H_{c2} (T) as a probe of anomalous normal state correlations in cuprates, Phys. C: Supercond. **235**, 2263 (1994).
[51] R. G. Dias and J. M. Wheatley, Upper critical field in a spin-charge-separated superconductor, Phys. Rev. B **50**, 13887 (1994).
[52] R. G. Dias, Effects of Van Hove singularities on the upper critical field, J. Phys.: Condens. Matter **12**, 9053 (2000).
[53] R. G. Dias, The upper critical field in the extended van-Hove scenario, Phys. B: Condens. Matter **294**, 492 (2001).
[54] N. Dupuis and G. Montambaux, Superconductivity of quasi-one-dimensional conductors in a high magnetic field, Phys. Rev. B **49**, 8993 (1994).
[55] N. Dupuis, G. Montambaux, and C. A. R. Sá de Melo, Quasi-One-Dimensional Superconductors in Strong Magnetic Field, Phys. Rev. Lett. **70**, 2613 (1993).
[56] N. Dupuis, Thermodynamics and excitation spectrum of a quasi-one-dimensional superconductor in a high magnetic field, Phys. Rev. B **50**, 9607 (1994).
[57] A. J. Leggett, Number-phase fluctuations in two-band superconductors, Prog. Theor. Exp. Phys. **36**, 901 (1966).
[58] D. F. Agterberg, E. Demler, and B. Janko, Josephson effects between multigap and single-gap superconductors, Phys. Rev. B **66**, 214507 (2002).
[59] P. J. W. Moll, X. Zhu, P. Cheng, H.-H. Wen, and B. Batlogg, Intrinsic Josephson junctions in the iron-based multiband superconductor $(V_2\,Sr_4\,O_6)\,Fe_2\,As_2$, Nat. Phys. **10**, 644 (2014).
[60] C. C. Sung, Magnetic properties of type-ii superconductors in the two-band model, Phys. Rev. **187**, 548 (1969).
[61] S. Peotta and P. Törmä, Superfluidity in topologically nontrivial flat bands, Nat. Commun. **6**, 8944 (2015).
[62] K. Noda, K. Inaba, and M. Yamashita, BCS superconducting transitions in lattice fermions, arXiv:1512.07858.
[63] K. Noda, K. Inaba, and M. Yamashita, Magnetism in the three-dimensional layered Lieb lattice: Enhanced transition temperature via flat-band and Van Hove singularities, Phys. Rev. A **91**, 063610 (2015).
[64] D. M. Kennes, L. Xian, M. Claassen, and A. Rubio, One-dimensional flat bands in twisted bilayer germanium selenide, Nat. Commun. **11**, 1124 (2020).
[65] M. Imada, A. Fujimori, and Y. Tokura, Metal-insulator transitions, Rev. Mod. Phys. **70**, 1039 (1998).
[66] L. P. Gorkov, The critical supercooling field in superconductivity theory, J. Exp. Theor. Phys. **10**, 593 (1960).
[67] A. A. Abrikosov, I. Dzyaloshinskii, and L. P. Gorkov, *Methods of Quantum Field Theory in Statistical Physics* (Dover, New York, 1975).
[68] A. L. Fetter and J. D. Walecka, *Quantum Theory of Many-Particle Systems* (Courier Corporation, New York, 2012).
[69] E. Pavarini, E. Koch, D. Vollhardt, and A. Lichtenstein, The Lanczos Method, *The LDA + DMFT Approach to Strongly Correlated Materials* (Forschungszentrum Jülich GmbH Institute for Advanced Simulations, Jülich, 2011), Vol. 1, Chap. 8, p. 8.1.